An immunoPET probe to SARS-CoV-2 reveals early infection of the male genital tract in rhesus macaques

Patrick J. Madden[1], Yanique Thomas[1], Robert V. Blair[2], Sadia Samer[1], Mark Doyle[2], Cecily C. Midkiff[2], Mark E. Becker[1], Muhammad S. Arif[1], Michael D. McRaven[1], Lacy M. Simons[3,4], Ann M. Carias[1], Elena Martinelli[1], Ramon Lorenzo-Redondo[3, 4], Judd F Hultquist[3,4], Francois J. Villinger[5], Ronald S. Veazey[2], and Thomas J. Hope[1*]

[1]Department of Cell and Developmental Biology, Feinberg School of Medicine, Northwestern University, Chicago, Illinois, USA

[2]Division of Comparative Pathology, Tulane National Primate Research Center, Covington, Louisiana, USA

[3]Department of Medicine, Division of Infectious Diseases, Northwestern University Feinberg School of Medicine, Chicago, IL, USA.

[4]Center for Pathogen Genomics and Microbial Evolution, Northwestern University Institute for Global Health, Chicago, IL, USA.

[5]New Iberia Research Center, University of Louisiana-Lafayette, New Iberia, Louisiana, USA

Abstract

Because of the recognized systemic nature of SARS-CoV-2 infection, a non-invasive and unbiased method is needed to clarify its spatiotemporal dynamics *in vivo* after transmission. We recently developed a probe based on the anti-SARS-CoV-2 spike antibody CR3022 to study SARS-CoV-2 pathogenesis *in vivo*. Herein, we describe its use in immunoPET to investigate SARS-CoV-2 infection of rhesus macaques. Using PET/CT imaging of macaques at different times post-SARS-CoV-2 inoculation, we demonstrate that the ^{64}Cu-labelled CR3022-F(ab')2 probe targeting the spike protein of SARS-CoV-2 can be used to study the dynamics of infection within the respiratory tract and uncover novel sites of infection. Differences in lung pathology between infection with the WA1 isolate and the delta variant were readily observed using immunoPET and corroborated CT lung pathology. The ability of the probe to illuminate lung-associated pathology demonstrates its specificity and function to detect infection in PET scan. The ^{64}Cu-CR3022-probe also demonstrated dynamic changes occurring between 1- and 2-weeks post-infection. Remarkably, a robust signal was seen in the male genital tract (MGT) of all three animals studied. Infection of the MGT was validated by immunofluorescence imaging of infected cells in the testicular and penile tissue and severe pathology was observed in the testes of one animal at 2-weeks post-infection. The results presented here underscore the utility of using immunoPET to study the dynamics of SARS-CoV-2 infection to understand its pathogenicity and discover new anatomical sites of viral replication. We provide direct evidence for SARS-CoV-2 infection of the MGT in rhesus macaques revealing the possible pathologic outcomes of viral replication at these sites.

PET/CT detected SARS-CoV-2 infection of 4 different tissues in the male genital tract illuminates the cause of COVID-19 clinical sequalae of male sexual health and fertility

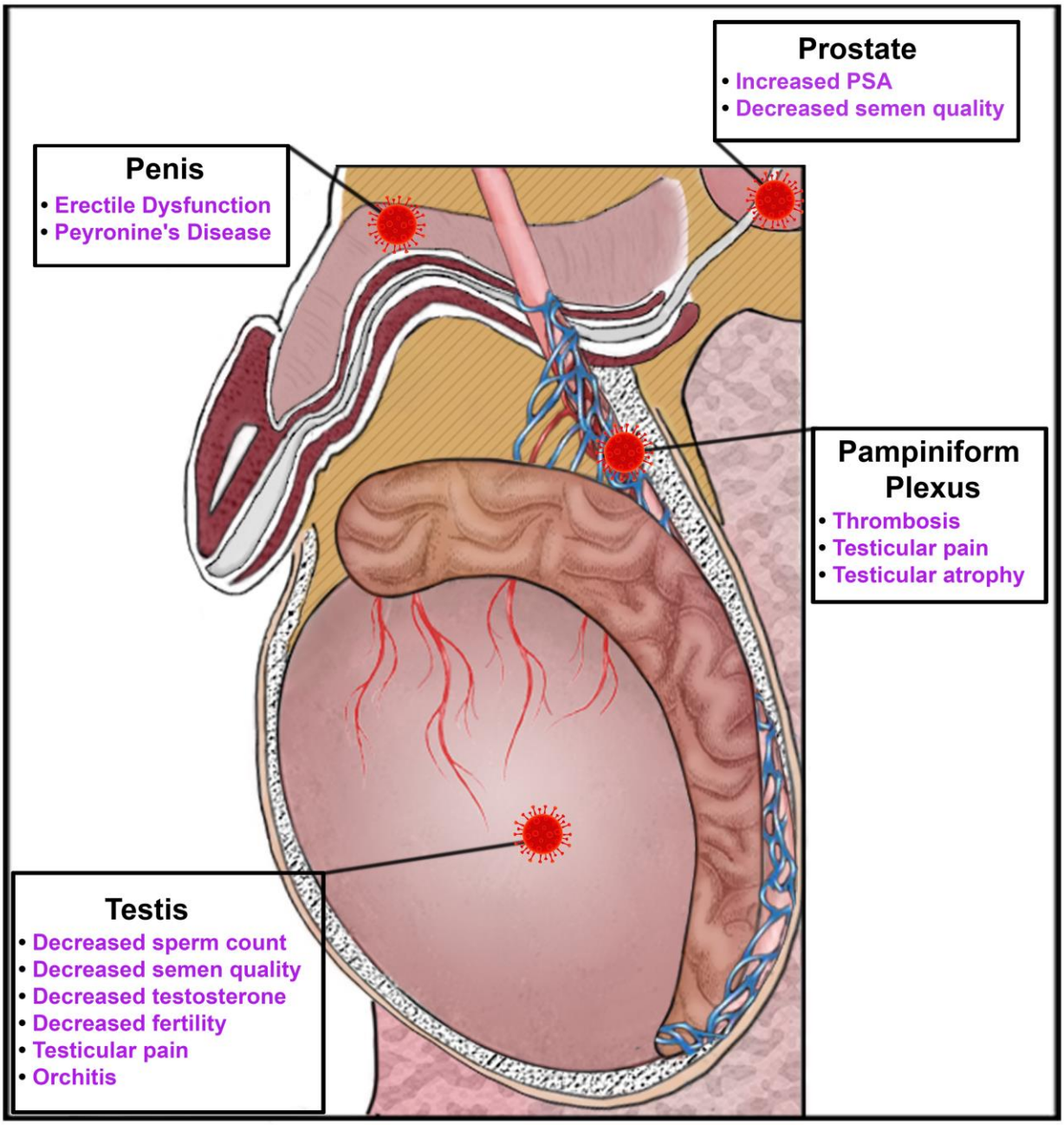

51 **Introduction**

52 The COVID-19 pandemic has exposed the broad systemic impact that can be caused by
53 infection with a respiratory virus. Disease associated with SARS-CoV-2 infection starts with
54 respiratory pathologies and subsequently can extend to other organ systems. There is now
55 ample evidence that SARS-CoV-2 can disseminate and replicate in tissues beyond the
56 respiratory tract. A clear example is infection in the gastrointestinal (GI) tract[1]. GI symptoms,
57 including diarrhea, have been reported by individuals with mild COVID-19, and hospitalized
58 patients have exhibited more severe symptoms such as ischemia and GI bleeds [2, 3,4]. In addition,
59 it is now well established that virus is shed through the GI tract in most infected individuals and
60 wastewater screening has become an important tool for disease surveillance[5, 6]. Although less
61 studied, many other tissues have been found to harbor SARS-CoV-2. Multiple groups have
62 shown the presence of viral RNA in cardiac, renal, and brain tissues[7-10]. There is also some
63 evidence of virus in the male genital tract (MGT) [11, 12]. Furthermore, symptoms associated with
64 all these organ systems have been regularly reported[13]. Likewise, other RNA viruses have
65 documented early dissemination to distal tissues that manifest infection-related pathology over
66 the long term, including (but not limited to) polio, mumps, Ebola, Zika, and SARS-CoV-1[14, 15]. For
67 example, studies of autopsy tissue from victims of SARS-CoV-1 suggested that it causes
68 inflammation of the testes (orchitis)[15]. However, it is not yet clear if the diverse pathologies
69 associated with SARS-CoV-2 infection are due to secondary effects of systemic inflammation or
70 direct infection of tissues at these distal sites. Human studies have relied on biopsies and
71 autopsy samples to investigate viral replication in sites other than the respiratory tract. The
72 biopsy/autopsy samples only offer a snapshot of the *in vivo* dynamics of disease, and there are

73 ethical and technical difficulties in obtaining them. Using animal models of infection allows for
74 a more thorough collection and investigation of affected tissues. To gain critical insights into
75 systemic infection by SARS-CoV-2, new animal models are needed to determine the extent of
76 disseminated infection and its relationship to pathogenesis.

77 SARS-CoV-2 infection in the non-human primate (NHP), rhesus macaques (*Macaca*
78 *mulatta*), recapitulates mild to moderate human disease[16-18]. Infected macaques exhibit viral
79 shedding through the respiratory tract and viral pneumonia similar to the mild form seen in
80 humans. The architecture of the respiratory tract is also generally conserved between humans
81 and macaques making them an ideal model for studying SARS-CoV-2 infection. Infection of
82 other organ systems has also been observed in macaques, most commonly in the GI tract[19, 20].
83 To gain insights into the spatiotemporal dynamics of SARS-CoV-2 during infection in the rhesus
84 macaque model, we adapted an immunoPET methodology that we are currently using to study
85 various aspects of simian immunodeficiency virus (SIV) acquisition and pathogenesis[21].
86 ImmunoPET is a molecular imaging technique that combines the specificity of an antibody-
87 based probe labeled with a radioisotope with the *in vivo* imaging power of combined positron
88 emission tomography-computed tomography (PET/CT). ImmunoPET was developed, and has
89 been used widely, in cancer research. Recently, with the advent of new antibodies and better
90 radioisotopes, immunoPET has been extended to studying many other biological processes[22, 23].
91 One of these areas is the study of the *in vivo* dynamics of pathogens such as bacteria, fungi, and
92 parasites. ImmunoPET allows for repeated and specific imaging of virally infected cells *in vivo* by
93 using a radioisotope labeled antibody targeting a viral protein. The non-invasive nature of
94 PET/CT imaging allows for unbiased discovery of novel tissue sites of infection through whole

95 body imaging. Furthermore, the cell-associated PET signal persists in tissue after necropsy and
96 as the tissue is dissected. It can be used to determine the precise location of infected cells in
97 radioactive probe-guided necropsy. We have previously reported the early development of an
98 *in vivo* antibody-based probe against SARS-CoV-2 utilizing fluorescent tagging of the F(ab')2 of
99 the anti-spike IgG CR3022[24]. CR3022 was one of the first monoclonal antibodies identified that
100 bound tightly to SARS-CoV-2. It was originally derived from an individual infected with SARS-
101 CoV-1 but also exhibits tight binding to the spike protein of SARS-CoV-2. Here we extend the
102 use of the F(ab')2 of the anti-spike IgG CR3022 labelled with Copper 64 (Cu^{64} for immunoPET
103 and targeted necropsy to study systemic SARS-CoV-2 infection in the rhesus macaque model.
104 As we previously reported (Madden et al), studies in SARS-CoV-2 infected rhesus
105 macaques were consistent with the intravenously (IV) injected probe being able to associate
106 with and accumulate in SARS-CoV-2 infected cells, as also seen in tissue culture[24]. Based on the
107 ability of the fluorophore labeled CR3022-F(ab')2 to reveal sites of SARS-CoV-2 infection within
108 macaque tissues, we extended these studies to utilize a $[^{64}Cu]^{-}$DOTA- labelled CR3022-F(ab')2
109 probe followed by detection in PET/CT scan. Here we report the results from a series of pilot
110 studies to evaluate the potential of this SARS-CoV-2 immunoPET approach to study COVID-19
111 dynamics in total body in rhesus macaques. Our results show the utility of this approach in
112 investigating SARS-CoV-2 pathogenesis in the respiratory tract and in uncovering novel
113 anatomical sites of infection. Interestingly, we detected a robust and dynamic signal in the MGT
114 including the prostate, penis, and testicles. This observation is consistent with emerging and
115 ongoing clinical observations of orchitis, oligo-/azoospermia, and erectile dysfunction and
116 reveals these comorbidities are likely a consequence of the direct viral infection of the tissues

117 of the MGT. The successful development of an immunoPET probe to study SARS-CoV-2 in the
118 rhesus macaque challenge model will allow longitudinal studies to gain insights into SARS-CoV-2
119 progression, dissemination, and the development of comorbidities.
120
121 **Results**
122 **Description of macaque studies and PET/CT-guided necropsy**
123 The basic process and workflow of the PET/CT guided necropsy method is shown in Fig 1A. The
124 PET/CT guided necropsy approach consists of three separate PET/CT scans that are used to map
125 probe signal at the whole animal, organ, and tissue levels. The first scan is done ~16-24 hours
126 after the injection of the radio labelled F(ab')2 probe allowing for movement into the tissues[21].
127 This whole-body PET/CT scan (Scan 1) identifies "hot" organs and tissue areas. These tissue
128 areas are then collected at necropsy immediately following the scan and subjected to a second
129 PET/CT scan (Scan 2). Tissues containing probe signal are then cut into small blocks, placed in
130 cryomolds, and then rescanned (Scan 3) to identify individual "hot" tissues/blocks that likely
131 contain foci of virally infected cells. These "hot" tissues can then be used for downstream
132 characterization including RNA quantification and different types of microscopic analyses
133 characterizing virally infected cells.
134 The SARS-CoV-2 pilot infection study design with 3 male rhesus macaques is shown in
135 Fig 1B. Based on our previous studies utilizing a fluorescently tagged F(ab')2 probe, we decided
136 to perform the first PET/CT scan 1 week after challenge. In the first study, we infected a male
137 rhesus macaque (LP14) with the WA1 isolate of SARS-CoV-2 and performed a single PET/CT
138 scan followed immediately by necropsy. In the second study, two male rhesus macaques were

139 infected with the Delta variant of SARS-CoV-2, and both underwent a PET/CT scan 1 week after
140 infection. One of the animals (IN22) was scanned twice after a single probe injection and
141 necropsied after the 2nd scan. The early scan of IN22 was done 3 hours after injection of the
142 ^{64}Cu-labelled F(ab')2 probe and a second whole-body scan was done ~21 hours after probe
143 injection with the PET/CT guided necropsy done immediately after. For the third animal (JF82),
144 the 1st PET/CT scan at week 1 post infection was done ~22 hours after IV probe administration
145 and was subsequently returned to its housing. On day 13, this same animal, JF82, was evaluated
146 at week 2 post-infection by whole-body scan 18 hours after probe administration, with
147 necropsy and subsequent scans moving efficiently with the now optimized workflows. These
148 initial studies revealed that the probe can identify sites of disseminated SARS-CoV-2 infection in
149 tissues beyond the respiratory tract.
150
151 **SARS-CoV-2 infection characteristics**
152 SARS-CoV-2 infection of the 3 animals was monitored via classical H&E evaluation of lesions in
153 lung tissue as shown in Fig 1C-E and via quantification of genomic and subgenomic RNA in nasal
154 swabs and saliva (Fig 1F, G). Pathology varied from minimal in LP14 (Fig 1C), to mild in JF82 (Fig
155 1E), and IN22 (Fig 1D). These findings are consistent with the pulmonary pathology of SARS-
156 CoV-2 infected rhesus macaques observed in other studies performed at the Tulane National
157 Primate Research Center[17, 25]. The pulmonary pathology consisted of variable interstitial
158 inflammation and type II pneumocyte hyperplasia (IN22 and JF82), which in the most severely
159 affected animal (IN22) also exhibited prominent atypia. Fig 1F and G shows the level of genomic

160 (Fig 1F) and subgenomic (Fig 1G) RNA in nasal swabs and saliva for all 3 animals. No significant
161 differences were noted in viral loads between the 3 animals.
162
163 **Distribution of SARS-CoV-2 signal after 1 week of infection with the WA1 isolate**
164 The three PET/CT scans of LP14, include the whole body (Fig 2A and B, S1-video), the organ scan
165 (Fig 2C, D, and E, S2-video) and the tissue scan (Fig 2F); these are shown at the top of Fig 2. Two
166 results immediately stood out relative to anticipated results. A minimal signal was associated
167 with the lungs, while a very strong signal was associated with the penis and testes of this
168 infected animal. To better evaluate the probe signal in the lungs, the 3D reconstruction of the
169 lungs was isolated from the PET datasets and the lung signal was projected over the CT
170 reconstruction of the skeleton as shown in Fig 2G and H (S3-video). The signal associated with
171 the lungs was diffuse and quite uniform throughout the tissue as observed in the whole animal
172 scan. This is more evident in the projection of the lung signal without CT as shown in Fig 2I and J
173 (S3-video). However, the lung signal was more evident in the post necropsy organ scan when
174 the intact respiratory tract including the tongue were scanned again (Fig 2C). In this case, the
175 lungs were no longer inflated within the body increasing signal density and leading to higher
176 overall signal in the 2nd scan. Two different respiratory tract z-series images, shown in Fig 2K
177 and L, reveal a focus of signal associated with the base of the tongue, overlapping with the
178 pharynx as evidenced by the cartilaginous structures seen in the CT. There were abundant small
179 foci of signal distributed throughout the lung tissue, often adjacent to the trachea and bronchi
180 as they branch out into the lungs. In addition, the z-series' reveal that the observed PET signal is
181 associated with the tissues and not with the open airways of the bronchus and ever narrowing

182 bronchi. Immunofluorescence microscopy revealed areas of infected cells lining alveoli in lung
183 tissue sections that had PET/CT signal (Fig 2M and N) confirming the specificity of the PET
184 signal.

185 In contrast to the weak, diffuse signal associated with the lungs, there was a strong and
186 more focal PET signal within the MGT as shown in the front (Fig 3A) and side (Fig 3B-C) views
187 (S4-video). The testes have a generally diffuse signal with some concentration of signal at the
188 dorsal and ventral surface of both LP14 testes. The MGT of the rhesus macaque is similar and
189 distinct to that of humans in several ways. Unique aspects of the penis are that it is primarily
190 retracted within the body within a prepuce and there is a small bone located within the glans
191 penis known as the baculum which is visible in the CT scan of the animals (Fig 3B and C, red
192 arrow). There was a very pronounced PET signal associated with the root of the penile tissues,
193 which is buried within the abdomen. The 3D PET signal was projected in green in a front (Fig
194 3D) and side view (Fig 3E) to better illustrate the signal associated with the MGT and to
195 visualize the signal from the root of the penis (see S5-video). The localization of the PET signal
196 for the penis and testes in the context of the skeletal CT signal is shown in three different
197 projections in panels 3F, 3H, and 3J, and isolated in panels 3G, 3I, and 3K (S6-video). The testis
198 overlays shown in Fig 3L-O reveal that the PET signal is primarily associated with the testis and
199 is distributed throughout the testicular tissue. There is also some potential signal associated
200 with the epididymis. This primary signal localization is also supported by the tissue scan (Fig 2F:
201 row 6 column 3, Fig S2) where the major PET signal is not associated with the epididymis
202 fragment in the piece of tissue.

203 In anticipation of a potential signal in the testes, which are known to express the SARS-
204 CoV-2 receptor ACE2, we had designated the testes to be a component of the organ scan post
205 necropsy. Unfortunately, much of the penis tissue was discarded at the necropsy of LP14
206 except for a small piece of penile tissue remaining within the abdomen. This small piece of
207 penile tissue retained PET signal as can be seen in Fig 2 (Fig 2F: row 8 column 5, Fig S2).
208 To extend our analysis of the testicular tissues of LP14, we evaluated tissue sections for
209 expression of SARS-CoV-2 proteins and host proteins using immunofluorescence microscopy to
210 potentially identify infected cells within the testicular tissue. As shown in Fig 4A, in LP14, ACE2
211 is expressed in the peritubular myoid and Sertoli cells surrounding/lining the base of the
212 seminiferous tubules. Next, we stained testicular tissue sections from LP14 with an anti-SARS-
213 CoV-2 guinea pig serum. Infected cells were evident in seminiferous tubules but were not
214 widely distributed and were instead localized in small clusters of cells at the base of the
215 seminiferous tubules (Fig 4B). Infection of Leydig and other interstitial cells could not be
216 evaluated due to loss of these cells during tissue processing. To further investigate the
217 phenotype of infected cells we stained with markers to help identify peritubular myoid cells
218 (smooth muscle actin) and Sertoli cells (vimentin). SARS-CoV-2 anti-serum colocalized with
219 vimentin staining at the base of the tubules, indicating that Sertoli cells are being infected (Fig
220 4C). However, SARS-CoV-2 staining was sometimes observed in cells negative for vimentin
221 indicating that cellular targets exist in addition to Sertoli cells (presumably germ cells) (Fig 4C,
222 arrow heads).
223
224

225 **Distribution of SARS-CoV-2 Delta variant signal after 1 week of infection**

226 Because of the mild disease manifestations of SARS-CoV-2 WA1 seen in many rhesus macaque
227 studies, the next set of animals were infected with the Delta variant which had become the
228 dominant circulating variant at the time of this study[26]. For IN22, at 1-week post infection, we
229 performed 2 PET/CT scans at 3- and 21-hours post probe injection to gain insights into the
230 dynamics of the probe distribution over time. This is an important aspect of probe function
231 because as the probe distributes from circulation into the tissue it will encounter virally
232 infected cells which will affect its distribution pattern. The three PET/CT scans of IN22, the
233 whole body (Fig 5A-D and S7-video, S8-video), the organ scan (Fig 5E-H and S9-video) and the
234 tissue scan (Fig 5I) are shown in Fig 5. The front and side views of the 3-hour scan (Fig 5A, B and
235 S7-video) and 21-hour scan (Fig 5C, D and S8-video) reveal a highly dynamic system of probe
236 distribution demonstrating that the timing of the PET/CT scan after probe injection is an
237 important consideration. The 3-hour scan clearly captures a robust probe signal in the
238 vasculature and chambers of the heart, consistent with a large fraction of the probe still
239 circulating in the blood after IV injection. A strong lung signal is apparent in the 3-hour scan in
240 contrast to the previous animal. In the 21-hour scan, the lung probe signal remained much
241 greater than observed in LP14 and was further distributed throughout the tissue. A very strong
242 signal was observed associated with the prostate in the 3-hour scan. The prostate signal
243 decreased substantially but was still strong in the 21-hour scan. Probe signal in the MGT was
244 also apparent at the 3-hour timepoint and was further amplified at 21-hours. For the most
245 part, an increase in signal was seen at tissue sites of probe labeling in the 21-hour scan. In
246 contrast, the vasculature signal decreased substantially, consistent with the movement of the

247 probe from blood, into tissues. However, some discrete probe labeling of certain vascular sites
248 remained, possibly indicating infection of the vasculature.
249 To better evaluate the probe signal in the lungs after Delta infection, the 3D
250 reconstruction of the IN22 lungs was isolated from the PET datasets and the lung signal was
251 projected over the CT reconstruction of the skeleton as shown in Fig 6A-D (S10-video). Both the
252 3-hour and 21-hour signals are significant and localized. The lung rotation series shown in Fig
253 6E, and F reveal a major signal associated with the caudodorsal portion of the right lung and
254 less signal associated with the left lung. Single z images of the PET and CT signal in sagittal and
255 transverse sections is shown in Figs 6G-J to better facilitate the analysis of the relationship of CT
256 revealed lung pathology with the PET signal. This comparison reveals an overlap of the opaque
257 lung signal and greater PET signal in the right lung in contrast to the more CT transparent left
258 lung tissue (Fig 6G-J). The stronger PET signal in the right lung observed in the whole-body scan
259 is recapitulated in the organ scan as shown in Fig 6K-O. This animal had overt gross pathology
260 associated with the dorsal areas of the right lower lung lobe as highlighted in the magnified
261 inset shown if Fig 6L. Histopathology of this region revealed marked pulmonary interstitial
262 inflammation and type II pneumocyte hyperplasia (Fig 1D, and 6P-S). The projection of the PET
263 signal over the photo (6N) shows a strong PET signal in multiple lung lobes and located adjacent
264 to the focally extensive areas of consolidation (red and inflamed areas). A similar strong PET
265 signal is observed in several areas of the left lung, with a major PET signal associated with the
266 caudal aspect of the upper lobe of the left lung. An overlay of the unnormalized PET over a CT
267 projection that reveals lung structure and fluid in the lung (6O) further details the relationship
268 between the areas with evidence of pneumonia and the PET signal. The PET signals tend to be

269 adjacent to opaque regions potentially caused by fluids and the regions of consolidation visible
270 in the photo. Next, we evaluated paraffin blocks of the right lower lobe by H&E (Fig 6P and R)
271 and immunofluorescent staining for SARS-CoV-2 (Fig 6Q and S). In regions of pneumonia (Fig
272 6P), the interstitium and alveolar spaces are expanded by inflammatory infiltrate. In these same
273 regions, SARS-CoV-2 infected cells are scattered throughout (Fig 6Q). Higher magnification
274 imaging of the H&E stain (Fig 6R) reveals the inflammatory infiltrate is composed predominately
275 of macrophages with fewer neutrophils (arrowheads). Alveolar septa are frequently lined by
276 type II pneumocytes (arrows). SARS-CoV-2 staining (Fig 6S) reveals infected cells within alveoli
277 (arrows) and lining alveolar septa (arrowheads). 2-color immunofluorescence staining for spike
278 and nucleocapsid can identify SARS-CoV-2 infected cells in the right lung (Fig 6T). Spectral
279 imaging confirmed that the fluorescence signal associated with the double positive cells is
280 consistent with the specific fluorophores utilized for antigen visualization. Additional
281 fluorescent staining shows focal nature of infected cells in a large piece of lung tissue (Fig 6U-
282 W). The 2-color imaging is a powerful method to validate the identification of SARS-CoV-2
283 infected cells. Spectral imaging of left lung tissue stained for NC and dsRNA is shown in panels
284 6X-Z. The spectrum shown in Fig 6Z confirms that the cells identified in panel 10Y are
285 specifically double stained with the antibodies to dsRNA and SARS-C0V-2 NC protein.
286 A comparison of the 3-hour and 21-hour PET/CT signal in the IN22 MGT is shown in Fig
287 7A-D. The isolated PET signal of the MGT of both scans is shown in Fig 7E-H. A signal is apparent
288 in the base of the testes that becomes more diffuse at the 21-hour timepoint. There is also a
289 signal apparent just above both testes in the 3-hour scan that increases at 21-hours and is most
290 prominent above the right teste (Fig 7A-H, indicated by white asterisk). Examination of both

291 scans indicates that the probe signal was initially associated with the vasculature, but it
292 persisted and accumulated adjacent to the top of testes in the 21-hour scan. This PET signal is
293 associated with the vasculature of the spermatic cord as is visible in the CT projections and the
294 PET overlays in the 21-hour scan (Fig 7I-L) and after the necropsy (Fig 7M-P). The post necropsy
295 signal matches the *in vivo* scan with the left testicle having a persistent signal throughout the
296 spermatic cord and a more localized signal on the top of the right testis. To confirm infection in
297 these tissues, the tissue block with the greatest PET signal (L Test 1, Fig 5I) was sectioned for
298 genomic and microscopic analysis. Bulk RNA was isolated from 2 tissue sections and qPCR
299 analysis of the SARS-CoV-2 N gene revealed the presence of viral RNA (2.03 Copies N1/µl, Table
300 S1). Immunofluorescence analysis of the PCR positive tissue derived from the same block
301 revealed the presence of sparse cells double positive for spike and nucleocapsid primarily found
302 in the interstitial space as shown in Fig 7Q and 7R. Staining of penile tissue from an uninfected
303 macaque is shown in Fig 7S and reveals robust ACE2 expression in the venous spaces of the
304 corpus cavernosum. Multiple SARS-CoV-2 infected cells in the penis were revealed by double
305 staining for nucleocapsid and dsRNA (J2) as shown in Fig 7T-W.
306
307 **Longitudinal analysis of SARS-CoV-2 Delta variant distribution 1- and 2-weeks post-infection**
308 For the final pilot study, we performed two longitudinal PET/CT scans, at 1- and 2-weeks post
309 challenge with the Delta variant, on a single animal (JF82). The goal of this study was to
310 determine if the ^{64}Cu-F(ab')2 probe could provide novel insights into the spatiotemporal
311 dynamics of SARS-CoV-2 infection with sequential PET/CT scans. A front and side view of the
312 sequential PET/CT scans at 1-week (Fig 8A-B) and 2-weeks (Fig 8C-D) reveals dynamic changes

313 in various organ systems. For example, there was a decrease in the signal of the lungs between
314 week one and two while MGT signal increases. These changes are illustrated in the front (Fig
315 8E) and side (Fig 8F) view overlay of the 1-week (shown in red) and 2-week (shown in blue)
316 timepoints. Areas with blue signal indicate increased signal in week 2 relative to week 1 and
317 areas with red signal indicate where the week 1 scan had greater signal. Areas with white signal
318 indicate where there is high PET signal overlapping in both scans. The post necropsy organ scan
319 (8G-J and S7-video) and the tissue scan (8K) are shown in Fig 8. Probe signal associated with
320 the lungs and MGT is visible in both the organ scan and the tissue scan.

321 To better compare the probe signal in the lungs of JF82 at the 1-week (Fig 9A-B) and 2-
322 week (Fig 9C-D) timepoints, the 3D reconstruction of the JF82 lungs was isolated from the PET
323 datasets and projected over the CT reconstruction of the skeleton (Fig 9A-D). Both the 1- and
324 2-week lung signals are significant and localized with a level of signal comparable to the
325 previous animal (IN22) infected with the Delta variant. An evaluation of the data set revealed a
326 PET signal overlying a region of opacity in the lower lobe of the left lung as designated with the
327 asterisks in several of the panels (Fig 9A-B, 9G-L). The lung rotation series shown for week 1 in
328 Fig 8E and week 2 in Fig 8F reveal a major signal associated with the dorsal side of the left lung
329 at both timepoints and less signal associated with the right lung in the week 1 scan. Evaluation
330 of signal from coronal sections of the week 1 PET/CT overlay (Fig 9G) and CT alone (Fig 9I)
331 reveals an overlap of the probe signal with an opaque region consistent with focal pneumonia.
332 It is notable that both the PET and CT signal associated with this spot in the left lung are gone in
333 the week 2 scan (Fig 9H and J). This is consistent with reports that the lung pathology observed
334 in the rhesus macaque model is most apparent after 1 week of infection and can wane by week

335 2[25]. The change between week 1 and week 2 is illustrated in Fig 9K and L where the week 1
336 scan is shown in red, and the week 2 scan is shown in blue and overlaid with the week 1 CT
337 signal. This change in the lung signal suggests that the ^{64}Cu-CR3022-F(ab')2-probe could be an
338 important tool to gain insights into the dynamics of SARS-CoV-2 infection and dissemination in
339 the rhesus macaque model. Microscopic analysis revealed pulmonary infiltrates were still
340 present in the alveolar space at necropsy (Fig 1E). However, no infected cells were detected
341 with immunofluorescence using an anti-SARS-CoV-2 antibody in FFPE tissue. These findings are
342 suggestive of a resolving infection which is supported by the histopathology (Fig 1E) and viral
343 RNA levels (Fig 1F and G).

344 We next evaluated the signal associated with the MGT of JF82 as illustrated in Fig 10A-E
345 which presents the front and near side view (~45˚) of the abdominal area of the week 1 (Fig 10A
346 and D), week 2 (10B and E), and overlay (10C and F). The overlay (Fig 10C and F) reveals the
347 dynamics of the probe signal in the MGT of JF82 in the first 2 weeks of SARS-CoV-2 infection.
348 The white signal in the overlay reveals that the probe signal is maintained in the prostate, the
349 vasculature at the base of the spermatic cord, and the base of the testes. To gain additional
350 insights into the MGT associated signal at the 2 time points, we isolated the MGT volumes and
351 3D projected the signal as shown in Fig 10G-J. In the week 1 scan (Fig 10G-H) a signal associated
352 with the root of the penis is also apparent in addition to the signal associated with the
353 vasculature at the base of the spermatic cord and the base of the testes. In the week 2 scan,
354 the signal becomes more diffuse, spreading throughout the penis and testes, and extending
355 into the spermatic cord, especially into the right spermatic cord. To better visualize the signals
356 associated with the different tissues, we isolated the volumes containing the penile signal for

357 the week 2 scan as shown in the projections presented in Fig 10K-M. The signal distribution
358 throughout the penis at week 2 is readily apparent and distinct from the signal associated with
359 the spermatic cord. It is notable that the probe signal associated with the MGT becomes better
360 distributed and more pronounced in the week 2 scan, consistent with a spreading infection in
361 the MGT between week 1 and week 2. In contrast, a focus of infection in the right lung (Fig 9)
362 of the same animal is observed in the week 1 scan and resolved in the week 2 scan.
363 Histopathology of testicular tissue from JF82 revealed multifocal regions of degenerate
364 seminiferous tubules characterized by a complete loss of germ cells and spermatids (Fig 10N).
365 These regions also have evidence of edema as revealed by increased spaces between individual
366 seminiferous tubules. Degenerate seminiferous tubules occasionally contained macrophages
367 with phagocytosed spermatids, and the adjacent interstitium was infiltrated by low numbers of
368 lymphocytes and plasma cells. To further characterize the degenerative changes noted on H&E,
369 immunofluorescence for CD206, a mannose receptor present on monocytes, macrophages[27],
370 and mature spermatids[28-30] and caspase 3, a cellular marker of apoptosis, was performed.
371 Degenerate seminiferous tubules were readily identified by the marked decrease in CD206
372 expression (due to loss of mature spermatids) and increased expression of caspase 3 compared
373 to adjacent, nondegenerate, tubules (Fig 10O, Q, R, and S). Evidence of intra-tubule
374 macrophages was readily apparent (Fig. 10R, S). SARS-CoV-2 infected cells can be identified in
375 the JF82 testes with triple staining for NSP8, nucleocapsid, and SARS-CoV-2 anti-sera shown in
376 Fig 10T and U.
377
378

379 **Comparison of PET signal between animals**

380 A comparison of the PET/CT scans of 3 SARS-CoV-2 infected rhesus macaques is revealing in
381 terms of the dynamics of infection and the utility of this technique to study COVID-19. In Fig
382 11A-D we present a comparative rotation series of the PET signal withing the lung volumes of
383 all scans. Although there are differences in the lung signal of each scan, the Delta variant
384 utilized for infection of IN22 (Fig 11B) and JF82 (Fig 11C-D) is associated with increased
385 pathology[26] (Fig 1C-E, Fig 5, and Fig 8) and increased PET signal (Fig 11B-D) without a clear
386 difference in viral load in nasal swab or saliva at 1 week after challenge (Fig 1F and G) compared
387 to LP14. This is consistent to similar viral loads between WA1 and the Delta variant in a recent
388 report[26].

389 The probe signal associated with the MGT was not anticipated, but apparent in all 3
390 animals. This reveals that infection of MGT is consistently seen in the rhesus macaque model of
391 SARS-CoV2 IN/IT challenge. A comparison of the isolated MGT PET signal from the four whole-
392 body PET scans of 3 SARS-CoV-2 infected rhesus macaques (Fig 11E-H) presented as a rotation
393 series further reveals the dynamics of SARS-CoV-2 after infection. The difference in MGT signal
394 between the animal infected with WA1 (LP14) and the animals infected with the Delta variant
395 (IN22 and JF82) at week 1 is much less pronounced than that seen in the lungs. In all 3 week 1
396 MGT scans the signal is asymmetrically distributed with diffuse signal throughout the testicles,
397 an increased signal at the base and top of the testes, and a signal associated with the root of
398 the penis (Fig 11E-G). The MGT PET signal is visibly increased in the week 2 scan relative to the
399 week one scan (Fig 11G, H) for JF82 indicating further spread of infection into the MGT at that
400 time. Another obvious difference between the week 1 whole-body PET scans is a variable signal

401 associated with the heart and liver as shown in Fig 11I-K. LP14 had a diffuse PET signal
402 throughout the liver (Fig 11I). In contrast, the IN22 PET signal (Fig 11J) was primarily localized
403 with the right side of the liver and in JF82 the PET signal (Fig 11K) was localized to the base of
404 the liver. Additionally, the extent of labeling of the heart is variable with JF82 and IN22 having a
405 greater signal than LP14 (Fig 11L).

406 To take advantage of the quantitative aspects of PET detection, we isolated the total
407 standard uptake value (SUV) of the PET signal associated with the CT defined volumes as
408 plotted in Fig 11L. The 3 animals scanned 1 week (W1) post SARS-CoV-2 challenge are
409 presented together for the whole-body (WB) scan signal and all evaluated tissues. The single
410 week 2 (W2) PET signal of JF82 is presented for comparison. The WB values for all scans are
411 clustered revealing the reproducible nature of evaluation of the PET signal. An increase in the
412 total SUV between week 1 and week 2 for the MGT and testes volumes is consistent with the
413 increase of signal suggested by visual inspection of the isolated tissues presented in Fig 10 and
414 Fig 11G and H.

415 Another relevant tissue with PET signal observed in all 3 animals is the prostate. Probe
416 labeling of the prostate first became apparent in the early PET scan (3 hour after injection) of
417 IN22 where it was among the strongest, non-kidney associated signals (Fig 5A and B).
418 Therefore, we reevaluated the PET/CT data sets for the 3 animals. As is illustrated in Fig 12A-F,
419 we were able to detect a signal associated with the prostate in all animals (marked by white
420 asterisks). An inset showing a sagittal slice of the PET/CT shows the localization of the prostate
421 within the small white circle for each animal. In Fig 12G-L we show the PET signal isolated
422 within the penile volume of the whole-body scan for IN22 1-week post infection (Fig 12G-I) and

423 2-weeks post infection for JF82 (Fig 12J-L). LP14 is excluded from this analysis because the
424 penile tissue was not collected. The same general distribution of PET signal is seen in the organ
425 scan of IN22 (Fig 12M) and JF82 (Fig 12N). The localization of the PET signal is further defined in
426 the tissue scan of the cryomolds shown with (Fig 12O and Q) and without (Fig 12P and R) PET
427 signal for each animal. There is PET signal associated with the penile tissue with a stronger
428 signal associated with the penile root of IN22 and the glans of JF82. This PET/CT guided
429 necropsy of the MGT reveals a persistent signal associated with the penile tissue of these 2
430 animals. All 3 animals had an apparent PET signal associated with the testes at the 1-week
431 timepoint and that signal increased in the testes in the week 2 scan as shown in the single
432 coronal PET/CT section shown in Fig 12Q-T and quantified in Fig 11L. The histopathologic
433 analyses of the testes from all three animals are shown in Fig 12S-U. Testicular degeneration
434 was noted in seminiferous tubules of JF82 (Fig 10N). Panels demonstrate normal
435 spermatogenesis or lack thereof in JF82 (Fig 10N, O, R, S).
436 In addition, all animals had a PET signal located at the top of each testicle, where the
437 spermatic cord connects with the testicle. A dissection of the rhesus macaque testicular
438 anatomy is shown in Fig 13A-C. The spermatic cord contains the vasculature supplying blood to
439 the testicles, the vas deferens which transports mature sperm produced in the testes, and the
440 cremaster muscle (Fig 13A). The position in natural context of the macaque penis, testes, and
441 spermatic cord are shown in Fig 13B. A magnified view of the vasculature of the pampiniform
442 plexus is shown in Fig 13C. As shown in the IN22 MGT PET/CT series (Fig 13D-G), there is a
443 major signal associated with the top of the testicles, especially the right testicle. A further
444 examination of this signal within the PET/CT data set shows it is located just above the testicle

445 in the yellow volume shown in Fig 13D-G. This yellow volume is overlapping with a vasculature
446 structure consistent with the pampiniform plexus visualized by CT (Fig 10G and B). The signal
447 associated with the pampiniform plexus and spermatic cord is seen in the 1-week scan of all
448 animals in front (Fig 13H, J, and L) and rotate 45˚ view (Fig 13I, K, and M) outside of the ovals
449 indicating the tetes. The signal associated with the pampiniform plexus and spermatic cord for
450 LP14 can be seen outside of the white ovals in Fig 13L-Q.
451
452 **Principal component analysis of PET SUV signals**
453 The PET signal includes several parameters in each anatomical areas, which provide different
454 insights into the distribution of the probe within the tissue. For example, the total SUV shown in
455 Fig. 11L, provides insights into the overall signal in each tissue/animal. However, the total SUV
456 does not account for variability in tissue size and shape. The mean SUV provides insights into
457 the relative intensity of PET signal in each tissue as shown in Fig. 14A. This comparison of mean
458 SUV reveals the relative intensity of the prostate signal amongst the highest signals detected in
459 all tissues. In contrast, the total SUV/whole body Total SUV for the different tissues illustrates
460 the percentages of the total whole-body signal in each tissue without consideration of the size
461 of each tissue relative to the other. All 7 PET parameters for each tissue are shown in the
462 Heatmap (Fig. 14C) which reveals that different tissues have unique signal characteristics. From
463 this analysis it is evident that the prostate signal of IN22 and JF82 have the highest mean SUV
464 and standard deviation with relatively a high median SUV being also seen in the prostate of the
465 3rd animal LP14. For example, the prostate signal of IN22 and JF82 has the highest mean SUV
466 and standard deviation with relatively a high median SUV being also seen in the prostate of the

467 3rd animal LP14, indicating a more clustered signal compared to the tissues with the highest
468 total SUV. To facilitate the use of our PET data to gain insights into our data set we utilized
469 Principal Component Analysis (PCA) followed by hierarchical clustering to examine the data
470 from all scans of the 3 animals. To cluster tissues according to their SUV signal characteristics,
471 we applied PCA including all variables obtained from the SUV measurements (i.e Total SUV,
472 Total SUV Whole Body ratio, Mean SUV, Median SUV, Standard Deviation SUV, Max SUV, and
473 Kurtosis) for each tissue and animal. After this analysis, we observed 4 different clusters that
474 correspond to tissues that display very distinct SUV signals. The clustering captures the prostate
475 signal described in the heat map where they are part of cluster 4 (dark blue group). Of note, the
476 major right lung signal of IN22 also clusters within this group (Fig 14D). The evident PET signal
477 observed in the lungs of the Delta variant animals IN22 and JF82 are part of the cluster 3 (green
478 group) (Fig 14D) revealing their similarity with its small foci of high signal and increased kurtosis
479 value (indicating data heavy tails or more outliers) consistent with the signal variability. The
480 higher kurtosis is also associated with penile and testes signal of all the animals in the red and
481 light blue clusters 1 and 2. This analysis allows us to begin to appreciate the nature of the PET
482 signal associated with the different tissues, different animals, different viruses, and identify
483 outliers.
484

485 **Discussion:**

486 The goal here was to develop a F(ab')2 based immunoPET probe to allow the visualization of
487 SARS-CoV-2 spike protein expression in the rhesus macaque infection model. This model is
488 clinically relevant as it was used to develop the highly successful vaccines now available against

489 SARS-CoV-2[31, 32]. The ability to detect anatomical sites of SARS-CoV-2 infection will facilitate
490 our understanding of COVID-19 disease severity and the mechanism of comorbidities in the
491 development of pathology. It could be especially useful in understanding long-COVID and its
492 underlying causes[33, 34]. This pilot study is a key step in the clinical development of this PET
493 probe to visualize SARS-CoV-2 replication and to facilitate treatments for COVID-19. The
494 distribution of the probe is complex, but it can reveal sites of SARS-CoV-2 infection in the rhesus
495 macaque model. The utility of the probe is best demonstrated by the temporal association of
496 the PET probe with CT detected lung pathology between weeks 1 and 2 in JF82. A PET signal
497 was clearly associated with an opaque region (pneumonia) in the left lung in the week 1 scan,
498 but both the PET signal and CT detected pneumonia are not present in the week 2 scan,
499 validating this technique. The overlays, shown in Fig 9, further illustrate this transient lung
500 pathology detected by comparing the two PET/CT scans separated by one week. Supporting
501 this interpretation of the PET/CT data, the pathology report shows that the left lung of JF82 has
502 type II pneumocyte hyperplasia and inflammatory infiltrate consistent with the normal course
503 of infection observed in the rhesus macaque model. Overall, the lung pathology associated
504 with SARS-CoV-2 in our three animals was consistent with the observation of many infected
505 rhesus macaques where the lung pathology was typically mild and peaked at 1 week after IN/IT
506 challenge. This dynamic was generally observed for lung associated signal in this limited pilot
507 study. There was some consolidation and inflammation observed in animal IN22 and this
508 coincided with an adjacent PET signal in both animals infected with the Delta variant.
509 Further validation of the PET/CT probe's ability to identify areas of infection at sites
510 other than the lungs and its utility in understanding COVID-19 pathogenesis was the revelation

511 of a highly reproducible infection of the MGT. This susceptibility of the MGT to infection with
512 SARS-CoV-2 may be an important consideration in the observation of higher mortality
513 associated with COVID-19 in men compared to women. In all three animals, the probe was
514 associated with the prostate, penis, pampiniform plexus, and testicles. We have been able to
515 identify SARS-CoV-2 infected cells in the testicles of all 3 animals. Comparing the longitudinal
516 PET scans of JF82 reveals that while the lung pathology and signal wane between week 1 and 2,
517 the signal of the MGT, and more specifically in the testicles increases in week 2. Consistent
518 with increased testicular infection at week 2 indicated in the PET scan, H&E staining of the JF82
519 testes revealed a unique pathology consisting of denuded stretches of the twisted and
520 intertwined seminiferous tubules (presenting as a tube cluster). Spermatids were absent in
521 these degenerate regions and the remaining Sertoli cells were undergoing apoptosis, seen
522 through caspase 3 staining (Fig. 10S). Local inflammation, or orchitis, was suggested by immune
523 infiltrates (Fig. 10R). Both the PET signal and pathology is greater in the left testicle of JF82.
524 Staining macrophages and mature spermatids for CD206 and all cells for caspase 3 activation
525 reveals a severe, acute response within short stretches of the seminiferous tubules where the
526 Sertoli cells are undergoing apoptosis due to inflammasome activation (caspase 3 activation),
527 and no spermatids are present consistent with an ongoing acute infection (Fig. 10N-S). We
528 have detected infected cells within the JF82 testes ((Fig. 10T, U) and the relationship between
529 the infected cells and testicular pathology is ongoing. Similar decreases in the cellular content
530 of the seminiferous tubules and sloughing of Sertoli cells and spermatids into the lumen have
531 been reported in multiple studies of autopsy tissues from COVID-19 related fatalities[35-40].

532 Our results suggest that SARS-CoV-2 rapidly and efficiently infects multiple tissues of the
533 male genital tract (MGT) early during infection in rhesus macaques. The complex vasculature
534 and known ACE2 expression of the tissues of the MGT make it a potential target of the virus[11,
535 41-43]. The SARS-CoV-2 infection of the testicles has been reported in mouse and hamster
536 respiratory challenge models[44-46]. Likewise, the testicles are also a target of Ebola and Zika virus
537 during systemic infection[47]. We observed a similar distribution of PET-probe signal in all 3
538 animals in the week 1 scan with labeling of the prostate, root of the penis, the top the testicles
539 and a second region of labeling at the base of the testicles (Fig. 11E-H). The signal above the
540 testicles localizes to the pampiniform plexus and vasculature of the spermatic cord while the
541 signal at the base of the testes is less clear but appears to be associated with the cauda
542 epididymis, which is the tail of the epididymis and serves as the storage site for mature sperm
543 and is highly vascularized. A further dissection of the testicles before the organ scan should
544 facilitate a detailed localization of the PET signal associated with the MGT in future studies.
545 There is also a signal associated with the testicles seen in all 3 animals along with infected cells
546 and associated pathology, especially in the one animal necropsied 2 weeks after challenge.
547 Although these studies were done with a rhesus macaque model, it is reasonable to
548 suggest that these observations may also apply to humans infected with SARS-CoV-2 because of
549 several clinical observations relating to male sexual health and fertility. It is highly relevant in
550 this extrapolation to consider that we have identified 4 distinct tissues where SARS-CoV-2
551 infection could impact male sexual health and fertility: SARS-CoV-2 infection of the prostate,
552 penis, pampiniform plexus, and testicles. The infection of the MGT and associated pathology
553 has been suggested by several publications and clinical studies. The prostate is known to be

554 ACE2 positive.[48] Interest in SARS-CoV-2 infection of the prostate has focused on two areas. First
555 is the potential impact on treatment of benign prostate hyperplasia[49] and prostate cancer [50]
556 with androgen deprivation therapy on the severity of COVID-19[51] and the potential impact of
557 SARS-CoV-2 infection on prostate cancer. It is notable that prostate cancers are known to
558 express high levels of transmembrane serine protease 2, TMPRSS2[52], which is known to activate
559 the SARS-CoV-2 spike protein to its optimal fusogenic potential[53]. Multiple studies have
560 explored this space and it does not appear that SARS-CoV-2 infection is associated with an
561 increase in prostate cancer[54]. In contrast, another study suggests that infection with SARS-CoV-
562 2 may be associated with an increase in prostate specific antigen (PSA) detection in plasma[55].
563 Future studies are needed to confirm whether the robust signal of the SARS-CoV-2 PET/CT
564 probe reflects a high-level infection of the human prostate and its subsequent impact on male
565 sexual health and fertility[56, 57]. SARS-CoV-2 infection of the penis is potentially associated with
566 the vasculature of the corpus cavernosum, which expresses high levels of ACE2 in the rhesus
567 macaque and human penile tissue (Fig, 7S) [43, 58]. Because the corpus cavernosum plays a key
568 role in erectile function, the inflammation caused by SARS-CoV-2 infection of the penile
569 vasculature is hypothesized to lead to erectile dysfunction (ED). This has indeed been reported
570 to be linked to COVID-19[43, 59, 60]. In addition, treatments for ED such as Viagra and Cialis are
571 known to affect the renin-angiotensin-aldosterone-system where ACE2 functions as a part of
572 the physiologic regulation of blood flow associated with normal erectile function[61].
573 A potential impact of COVID-19 infection on the pampiniform plexus might be suggested
574 by several case reports of COVID-19 associated thrombosis located in the pampiniform plexus[62-
575 65]. Additionally, the signal distribution of the left and right testes is distinct, with the signal of

576 the right testicle being more focused at the top of the testicle while the signal on the left
577 testicle being more distributed in the spermatic cord. This is reminiscent of the condition
578 known as varicocele, which manifests as varicose veins of the scrotum, and is prominent in the
579 left testicle relative to the right testicle[66]. This is due to the left testicle receiving its blood flow
580 from the left renal vein which exposes it to higher blood pressure and slower blood flow[67]. This
581 difference could be insightful if confirmed in more animals.

582 The potential infection of the testicles by SARS-CoV-2 could be highly impactful on male
583 fertility, potentially decreasing sperm count and semen quality[47, 68-70]. It is known that SARS-
584 CoV-2 infection in humans is associated with oligo- and azoospermia and a transient decrease
585 in fertility after infection[36, 38, 66, 68, 71, 72]. One study found that fertility amongst infected men
586 was reduced and returned to baseline 3-6 months after SARS-CoV-2 infection[73]. This decrease in
587 fertility was not seen in infected women or men who received a SARS-CoV-2 vaccination. We
588 find that the pathology associated with the testicles in the week 2 necropsy is extreme, with
589 apparent ablation of sperm production within short regions of the seminiferous tubules and
590 with accompanying immune infiltration consistent with an emerging COVID-19 associated
591 orchitis[64, 74]. Because of the four distinct mechanisms negatively impacting human male sexual
592 health and fertility, and the observation of all four mechanisms in all animals evaluated to date,
593 we feel compelled to report this information at this early stage of study and evaluation.

594 The results generated in this first study of an ^{64}Cu-labelled F(ab')2 probe reveal an
595 unexpected but reproducible infection of multiple tissues of the MGT. This observation
596 provides possible mechanistic insights into the mounting evidence that SARS-CoV-2 can impact
597 sexual health and fertility in infected men. Multiple studies have reported a decrease in

598 testosterone after SARS-CoV-2 infection[56, 75, 76]. Leydig cells, which produce testosterone, are
599 known targets of SARS-CoV-2[35, 37, 77]. The decrease in testosterone correlates with disease
600 severity[76, 78]. The direct infection of the testicles observed in the NHP studies presented here
601 are consistent with the MGT pathology reported in men[35-40]. The infection of the MGT may be
602 a common outcome in SARS-CoV-2 infection. We suggest further study in mild, and even in
603 asymptomatic infection, in men and macaques is clearly required.
604 Using a novel ^{64}Cu-labelled F(ab')2 probe targeting the SARS-CoV-2 spike protein, we
605 have found that it is possible to identify sites of SARS-CoV-2 infection in the rhesus macaque
606 infection model using a PET/CT scan. The rapid and consistent spread of SARS-CoV-2 infection
607 to the MGT in the first week of infection in the rhesus macaque suggests this could be an
608 important post pandemic health consideration as those infected during the pandemic develop
609 advanced disease and other manifestations of long COVID-19. Currently, there is no other
610 methods that allows for the unbiased discovery of novel anatomical sites of SARS-CoV-2
611 infection. We believe the immunoPET technique described here will be an important addition
612 to the toolkit for studying and understanding SARS-CoV-2 pathogenesis. The availability of an
613 immunoPET probe to SARS-CoV-2 in the clinical setting has the potential to reveal the
614 underlying role of disseminated viral infection in long COVID and could guide therapeutic
615 interventions to resolve SARS-CoV-2 related sequalae which could be a major health concern
616 for the lifetimes of those infected during the COVID-19 pandemic.
617
618
619

620 **Acknowledgements**

621 This work was supported by a NOSI supplement (R37AI094595-10S1 PI: Hope) to parent grant
622 R37AI094595 (PI Hope). We would like to thank Nicholas Maness for supplying the delta
623 variant virus and, Maury Duplantis, Brooke F. Gasperge, Kasi E. Russell-Lodrigue, and the
624 Veterinary team at TNPRC. Thanks to Richard D'Aquila for critical reading and editing of the
625 manuscript.

626

627 **Material and Methods**

628 **Preparation of F(ab)2**

629 CR3022-IgG1 was acquired from Absolute Antibody (#Ab01680-10.0, Absolute Antibody). The
630 IgG1 was digested into F(ab)2 as previously described. Briefly, a Genovis FragIT antibody
631 digestion kit (#A2-FR2-100, Genovis) was used according to manufacturer's protocol. CR3022
632 was digested by adding to the FragIT column and rocking for 1 hr at room temperature. The
633 column was then centrifuged to elute fragments. Fc fragments were removed after incubation
634 with the CaptureSelect Fc Column. F(ab')2 fragments were eluted from this column and size
635 was confirmed using SDS-PAGE.

636

637 **DOTA Labeling of Antibody**

638 CR3022-F(ab)2 was labeled with the chelator dodecane tetraacetic acid (DOTA) for the
639 attachment of ^{64}Cu. Chelex 100 chelating resin (#142-1253, BioRad) was used to prepare two
640 buffers: 0.1M sodium phosphate (pH 7.3) and 0.1M ammonium acetate (pH 5.5). Five grams of
641 Chelex was added to 100ml of each buffer and stirred at room temperature for 1 hour. Buffers

642 were then filter sterilized using 0.22 uM filters. CR3022-F(ab')2 was buffer exchanged into the
643 prepared 0.1 M sodium phosphate using Zeba columns (ThermoFisher, USA). DOTA-NHS-ester
644 (#B-280, Macrocyclics) was dissolved in dimethyl sulfoxide (DMSO) at a concentration of 10mM.
645 A 1:10 dilution of 1M sodium bicarbonate was made into a tube containing F(ab')2 in sodium
646 phosphate and 10mM DOTA was added at a molar ratio of 5:1. The tube was mixed and left to
647 rock at 37C for 1.5 hours. The labeled F(ab')2 was then buffer exchanged into fresh 0.1 M
648 sodium phosphate using a Zeba column.
649
650 **^{64}Cu labeling**
651 Before labeling DOTA conjugated F(ab')2 was buffer exchanged into freshly prepared 0.1M
652 ammonium acetate (pH 5.5) prepared with Chelex 100 using 10kDa cutoff Amicon centrifugal
653 microfilters (Cork, IRL). Cu^{64} chloride was obtained from Washington University, St. Louis MO
654 and shipped overnight to TNPRC. All work with Cu^{64} was performed inside a lead castle. The
655 radioactivity of the Cu^{64} was measured using an Atom Force 500 dose calibrator and recorded.
656 Next the Cu^{64} was added to a tube containing the DOTA labeled F(ab')2 in 0.1 M ammonium
657 acetate and incubated at 37°C for 1 hour while rotating. The labeled F(ab')2 probe was then
658 separated from unlabeled Cu^{64} and buffer exchanged into PBS via sequential centrifugation
659 steps using 10kDa cutoff Amicon centrifugal microfilters to a final volume of ~20µl. The
660 conjugated probe was then diluted to the final volume in PBS in sterile glass vials and drawn
661 into single dose syringes. Each dose typically labelled in the 1-3 mCi per dose.
662
663

664 **Animals and virus**

665 The virus used for experimental infection of LP14 was SARS-CoV-2; 2019-nCoV/USA-WA1/2020
666 (*https://www.ncbi.nlm.nih.gov/nuccore*; accession number MN985325.1) obtained from BEI
667 resources (BEI #NR-52281). Virus stock was prepared in Vero E6 cells and sequence confirmed
668 by deep sequencing. Plaque assays were performed in Vero E6 cells. Vero E6 cells were
669 acquired from ATCC (Manassas, VA). The virus used for experimental infection of IN22 and JF82
670 was SARS-CoV-2; hCoV-19/USA/MD-HP05647/2021 (Lineage B.1.617.2; Delta variant) obtained
671 from BEI resources (BEI #NR-55672). Delta variant stock was expanded using Calu-3 cells and
672 prepared as above using Vero E6 cells.

673 Three male rhesus macaques (Macaca mulatta) were used in this study. All animals were
674 housed at the Tulane National Primate Research Center (TNPRC, Covington, LA) which is
675 accredited by the Association for the Assessment and Accreditation of Laboratory Animal Care.
676 All procedures were reviewed and approved by the Tulane University Institutional Animal Use
677 Committee under protocol number P0452.One animal was inoculated with $1.1x10^6$ tissue
678 culture infectious dose ($TCID_{50}$) of the WA1 strain of SARS-CoV-2 via concomitant
679 intratracheal/intranasal instillation (1mL intratracheal, 500µL per each nare). This animal was
680 necropsied 8 days post-infection. The remaining two animals were inoculated with $1.12x10^6$
681 $TCID_{50}$ of the delta variant of SARS-CoV-2 via the same route. One animal was necropsied at day
682 7 and one at day 14 post-infection. All animals were intravenously infused with 0.5 mg/kg of
683 the radiolabeled F(ab')2 probe and JF82 was infused on two separate occasions. Macaque LP14
684 received 4 mCi, JF82 and IN22 received 1.3 and 1,4 mCi respectively on Dec 9, and JF82 received
685 an additional dose of 0.7 mCi on Dec 15. LP14 had nasal and salivary swabs taken at day 7. IN22

686 had swabs taken at days 3, 5, and 7 post-infection, while JF82 had swabs taken at days 3, 5, 7,
687 and 14.
688
689 **PET/CT Imaging and Necropsy**
690 PET/CT guided necropsies were performed in three sequential phases each separated by a
691 PET/CT followed by a period of analysis and sampling (1. whole-body, 2. organ, and 3. tissue).
692 First, whole-body scans were acquired prior to sending the animal to necropsy. Following
693 euthanasia, all major organ systems were removed (pluck, gastrointestinal tract, liver, spleen,
694 kidneys, urinary bladder, testicles, penis, prostate, seminal vesicles, nasal turbinate, lymph
695 nodes, carotid artery, cervical spinal cord, and brain) placed in a clear, plastic, sealable
696 container and sent back to PET/CT for an "organ scan". After the organ scans were
697 reconstructed, "hot" regions of each major organ (as seen on the organ scan) were sampled
698 and placed in cryomolds. The final "tissue" scan was acquired by placing the cryomolds in a
699 clear, plastic, sealable container and scanning them with the PET/CT. Following acquisition of
700 the tissue scan, cryomolds were filled with OCT and frozen on dry ice. All remaining tissue (not
701 placed in cryomolds) was placed in zinc-formalin fixative. All samples were stored for 5 days
702 before being removed from containment.
703
704 **PET/CT Image Analysis**
705 Acquired PET/CT whole-body images were analyzed using the MIM Software (MIM Software
706 Inc., Cleveland, OH). The PET and CT scans were reconstructed using the software and PETCT
707 fusions were created to analyze regions of interest through axial, sagittal, and coronal views.

The PET scans were presented in calculated Standardized Uptake Values, and all images were set to the same scale (0-20 SUVbw). The PET scale was selected based on the overall signal intensity of the PET scans, and the CT scale for optimal visibility of the tissues. Regions of interest (ROI) were isolated using a combination of the Region Grow function and manual contouring on a representative scan, then these regions were copied on subsequent scans of the same animal using a specialized developed workflow. This workflow allows the software to use the CT scans to map the selected ROI and locate that exact volume in subsequent scans. Manual adjustments were then used to counter any changes in the animals' orientation between scans. The areas within these regions were then extracted from the full scans, and the anatomical regions were analyzed in both 2D cross-sections and 3D projections. 3D views are maximum intensity projections of isolated ROI in the PET scans.

To cluster tissues according to their SUV signal characteristics, we used Principal Component Analysis (PCA) where we included all variables obtained from the SUV measurements (i.e Total SUV, Total SUV Whole Body ratio, Mean SUV, Median SUV, Standard Deviation SUV, Max SUV, and Kurtosis) for each tissue and animal. The clustering of each tissue was subsequently obtained by agglomerative hierarchical clustering on the PCA results. After building an initial hierarchical tree, the sum of within-cluster inertia was calculated for each partition. The selected partition was the one with the higher relative loss of inertia. Both PCA and agglomerative hierarchical clustering were performed using FactoMineR package and factoextra was used for visualization of the clustering results.

730 **Isolation and Quantification of viral RNA**

731 Viral load was quantified from pharyngeal and nasal swabs taken from infected animals at
732 TNPRC as previously described (1) Swab and bronchial brush samples were collected in 200 µL
733 of DNA/RNA Shield 1× (catalog number R1200; Zymo Research, Irvine, CA) and extracted for
734 viral RNA using the Quick-RNA viral kit (catalog number R1034/5; Zymo Research). The Viral
735 RNA Buffer was dispensed directly to the swab in the DNA/RNA Shield. A modification to the
736 manufacturers' protocol was made to insert the swab directly into the spin column to
737 centrifugate, allowing all the solution to cross the spin column membrane. The viral RNA was
738 then eluted (45 µL) from which 5 µL was added in a 0.1-mL fast 96-well optical microtiter plate
739 format (catalog number 4346906; Thermo Fisher Scientific, Waltham, MA) for a 20-µL real-time
740 quantitative RT-PCR (RT-qPCR) reaction. The RT-qPCR reaction used TaqPath 1-Step Multiplex
741 Master Mix (catalog number A28527; Thermo Fisher Scientific) along with the 2019-nCoV RUO
742 Kit (catalog number 10006713; IDTDNA, Coralville, IA), a premix of forward and reverse primers
743 and a FAM-labeled probe targeting the N1 amplicon of the N gene of SARS2-nCoV19
744 (https://www.ncbi.nlm.nih.gov/nuccore; accession number MN908947). The reaction master
745 mix was added using an X-stream repeating pipette (Eppendorf, Hauppauge, NY) to the
746 microtiter plates, which were covered with optical film (catalog number 4311971; Thermo
747 Fisher Scientific), vortexed, and pulse centrifuged. The RT-qPCR reaction was subjected to RT-
748 qPCR at a program of uracil-DNA glycosylase incubation at 25°C for 2 minutes, room
749 temperature incubation at 50°C for 15 minutes, and an enzyme activation at 95°C for 2 minutes
750 followed by 40 cycles of a denaturing step at 95°C for 3 seconds and annealing at 60°C for 30
751 seconds. Fluorescence signals were detected with a QuantStudio 6 Sequence Detector (Applied

752 Biosystems, Foster City, CA). Data were captured and analyzed with Sequence Detector
753 Software version 1.3 (Applied Biosystems). Viral copy numbers were calculated by plotting Cq
754 values obtained from unknown (ie, test) samples against a standard curve that represented
755 known viral copy numbers. The limit of detection of the viral RNA assay was 10 copies per
756 reaction volume. A 2019-nCoV–positive control (catalog number 10006625; IDTDNA) was
757 analyzed in parallel with every set of test samples to verify that the RT-qPCR master mix and
758 reagents were prepared correctly to produce amplification of the target nucleic acid. A non-
759 template control was included in the qPCR to ensure that there was no cross-contamination
760 between reactions.

761 OCT embedded tissue blocks were sectioned between 10-15 µM and 2-4 sections were
762 placed into RNAse free tubes. RNA extraction was carried out using a RNeasy Plus Mini Kit
763 (#74124, Qiagen), according to manufacturer's protocol. Briefly, 350µl of lysis buffer with
764 dithiothreitol (DTT) was added to the tubes containing sections. The tubes were vortexed
765 briefly then frozen at -20°C. Once thawed the samples were again vigorously vortexed then
766 centrifuged for 3 minutes. Supernatant was removed and applied to the gDNA Eliminator spin
767 column. The flow-through was mixed with 350µl of 70% ethanol and added to an RNeasy spin
768 column. The spin column was washed three times with buffers RW1 and RPE. RNA was then
769 eluted using 30-50µl of RNAse free water. All steps prior to addition of lysis buffer were carried
770 out in a BSL3 facility.

771

772

773

774 **Tissue Processing and H&E Staining**

775 Tissue samples were collected in Zinc formalin (Anatech) and fixed for a minimum of 72 hours
776 before being washed and dehydrated using a Thermo Excelsior AS processor. Upon removal
777 from the processor, tissues were transferred to a Thermo Shandon Histocentre 3 embedding
778 station where they were submersed in warm paraffin and allowed to cool into blocks. From
779 these blocks, 5µM sections were cut and mounted on charged glass slides, baked overnight at
780 60°C, and passed through Xylene, graded ethanol, and double distilled water to remove paraffin
781 and rehydrate tissue sections. A Leica Autostainer XL was used to complete the
782 deparaffinization, rehydration and routine hematoxylin and eosin stain. Slides were digitally
783 imaged with a NanoZoomer S360 (Hamamatsu) and subsequently examined by a board-
784 certified, veterinary pathologist using HALO software (Indica Labs).

785

786 **Fluorescent Immunohistochemistry of FFPE tissues**

787 Five µM sections of Formalin-fixed, paraffin-embedded (FFPE) tissues were mounted on
788 charged glass slides, baked for two hours at 60°C, and passed through Xylene, graded ethanol,
789 and double distilled water to remove paraffin and rehydrate tissue sections. A microwave was
790 used for heat induced epitope retrieval. Slides were heated in a high pH solution (Vector Labs
791 H-3301), rinsed in hot water, and transferred to a heated low pH solution (Vector Labs H-3300)
792 where they were allowed to cool to room temperature. Sections were washed in a solution of
793 phosphate-buffered saline and fish gelatin (PBS-FSG) and transferred to a humidified chamber,
794 for staining at room temperature. Lung sections were blocked with 10% normal goat serum
795 (NGS) for 40 minutes, followed by a 60-minute incubation with the anti-SARS primary antibody

796 diluted in NGS. Slides were washed and transferred back to the humidified chamber for a 40-
797 minute incubation with the secondary antibody, also diluted in NGS. Sequential staining of FFPE
798 testes, for CD206 and Caspase 3, was done as described above with 1% normal donkey serum
799 (NDS) being used in place of NGS for blocking and antibody dilutions. DAPI was used to label the
800 nuclei of each section. Slides were mounted using a homemade anti-quenching mounting
801 media containing Mowiol (Calbiochem #475904) and DABCO (Sigma #D2522) and imaged at
802 20X with a Zeiss Axio Slide Scanner.
803

PRIMARY ANTIBODY	SPECIES	COMPANY	CATALOG	DILUTION	SECONDARY ANTIBODY
SARS	Guinea Pig	BEI	NR-10361	1:1000	Goat anti-guinea pig Alexa Fluor488
CD206	Goat	R&D Systems	AF2532	1:50	Donkey anti-goat Alexa Fluor488
Caspase 3	Rabbit	Abcam	Ab13847	1:200	Donkey anti-rabbit Alexa Fluor555
Dapi		Invitrogen	D1306	1:20,000	

804

805 **Fluorescence Microscopy of OCT embedded tissues**

806 OCT embedded tissue were cryosectioned in a BSL3 facility between 10 and 15 µM. One or two
807 sections of each tissue were placed on glass microscope slides. Tissues were placed into an
808 airtight container containing 4% PFA in PIPES buffer. The container was sealed and thoroughly
809 decontaminated before being removed from the BSL3 facility. The remainder of the staining
810 took place outside of the BSL3. Tissue sections were treated with L-lysine (0.1%, SigmaAldrich)
811 to reduce background and non-specific interactions before being blocked using 3% BSA

812 (Invitrogen, ThermoFisher) for 30 minutes at room temperature. Staining with primary
813 antibodies was carried out at 37°C and secondary antibodies at room temperature. each for
814 1hr. Table of primary and secondary antibodies used is below. All slides were stained with
815 Hoechst (1:25,000, ThermoFisher, USA) for 15 minutes and washed with PBS between all steps.
816 Dako fluorescent mounting medium (#S302380-2, Agilent, USA) was used to mount cover slips
817 which were sealed with nail polish. A DeltaVision Ultra inverted microscope (Cytivia, USA) was
818 used to obtain images using the 10x, 20x, 60x, and 100x lenses. Images were deconvolved,
819 stitched, and projected using the softWoRx software (Applied Precision, USA).

Clone	**Antibody**	**Target**	**Company**	**Catalog#**	**Dilution**
	Rb pAb	Spike	Abcam	Ab272504	1:200
3A2	Ms mAb	Spike	Abcam	Ab272420	1:200
6H3	Ms mAb	NC	GeneTex	GTX632269	1:200
5A10	Ms mAb	NSP8	GeneTex	GTX632696	1:200
	Rb pAb	NC	Novus Biologicals	NB100-56576	1:200
	Rb pAb	NC	GeneTex	GTX135357	1:200
rJ2	Ms.mAb j2	Anti double stranded RNA	Millipore Sigma	MABE1134	1:1000

820
821
822
823
824
825
826
827

828 **References**

829 1. Cheung CCL, Goh D, Lim X, Tien TZ, Lim JCT, Lee JN, Tan B, Tay ZEA, Wan WY, Chen EX,
830 Nerurkar SN, Loong S, Cheow PC, Chan CY, Koh YX, Tan TT, Kalimuddin S, Tai WMD, Ng JL, Low
831 JG-H, Yeong J, Lim KH. Residual SARS-CoV-2 viral antigens detected in GI and hepatic tissues
832 from five recovered patients with COVID-19. Gut. 2021. doi: 10.1136/GUTJNL-2021-324280.
833 2. Kariyawasam JC, Jayarajah U, Riza R, Abeysuriya V, Seneviratne SL. Gastrointestinal
834 manifestations in COVID-19. Trans R Soc Trop Med Hyg. 2021;115(12):1362-88. doi:
835 10.1093/trstmh/trab042. PubMed PMID: 33728439; PMCID: PMC7989191.
836 3. Keshavarz P, Rafiee F, Kavandi H, Goudarzi S, Heidari F, Gholamrezanezhad A. Ischemic
837 gastrointestinal complications of COVID-19: a systematic review on imaging presentation. Clin
838 Imaging. 2021;73:86-95. Epub 20201208. doi: 10.1016/j.clinimag.2020.11.054. PubMed PMID:
839 33341452; PMCID: PMC7837247.
840 4. Javadekar NS. Gut in COVID 19-is it worth noticing. Ind Psychiatry J. 2021;30(Suppl
841 1):S267-S9. Epub 20211022. doi: 10.4103/0972-6748.328826. PubMed PMID: 34908706;
842 PMCID: PMC8611584.
843 5. Paterson BJ, Durrheim DN. Wastewater surveillance: an effective and adaptable
844 surveillance tool in settings with a low prevalence of COVID-19. Lancet Planet Health.
845 2022;6(2):e87-e8. doi: 10.1016/S2542-5196(22)00009-2. PubMed PMID: 35150632; PMCID:
846 PMC8828367.
847 6. Gregory DA, Wieberg CG, Wenzel J, Lin CH, Johnson MC. Monitoring SARS-CoV-2
848 Populations in Wastewater by Amplicon Sequencing and Using the Novel Program SAM Refiner.
849 Viruses. 2021;13(8). Epub 20210819. doi: 10.3390/v13081647. PubMed PMID: 34452511;
850 PMCID: PMC8402658.
851 7. Nakamura Y, Katano H, Nakajima N, Sato Y, Suzuki T, Sekizuka T, Kuroda M, Izutani Y,
852 Morimoto S, Maruyama J, Koie M, Kitamura T, Ishikura H. SARS-CoV-2 is localized in
853 cardiomyocytes: a postmortem biopsy case. Int J Infect Dis. 2021;111:43-6. Epub 20210809. doi:
854 10.1016/j.ijid.2021.08.015. PubMed PMID: 34384897; PMCID: PMC8351278.
855 8. Lei J, Liu Y, Xie T, Yao G, Wang G, Diao B, Song J. Evidence for residual SARS-CoV-2 in
856 glioblastoma tissue of a convalescent patient. Neuroreport. 2021;32(9):771-5. doi:
857 10.1097/WNR.0000000000001654. PubMed PMID: 33994523.
858 9. Song E, Zhang C, Israelow B, Lu-Culligan A, Prado AV, Skriabine S, Lu P, Weizman OE, Liu
859 F, Dai Y, Szigeti-Buck K, Yasumoto Y, Wang G, Castaldi C, Heltke J, Ng E, Wheeler J, Alfajaro MM,
860 Levavasseur E, Fontes B, Ravindra NG, Van Dijk D, Mane S, Gunel M, Ring A, Kazmi SAJ, Zhang K,
861 Wilen CB, Horvath TL, Plu I, Haik S, Thomas JL, Louvi A, Farhadian SF, Huttner A, Seilhean D,
862 Renier N, Bilguvar K, Iwasaki A. Neuroinvasion of SARS-CoV-2 in human and mouse brain. J Exp
863 Med. 2021;218(3). doi: 10.1084/jem.20202135. PubMed PMID: 33433624; PMCID:
864 PMC7808299.
865 10. Hanley B, Naresh KN, Roufosse C, Nicholson AG, Weir J, Cooke GS, Thursz M, Manousou
866 P, Corbett R, Goldin R, Al-Sarraj S, Abdolrasouli A, Swann OC, Baillon L, Penn R, Barclay WS,
867 Viola P, Osborn M. Histopathological findings and viral tropism in UK patients with severe fatal
868 COVID-19: a post-mortem study. Lancet Microbe. 2020;1(6):e245-e53. Epub 20200820. doi:
869 10.1016/S2666-5247(20)30115-4. PubMed PMID: 32844161; PMCID: PMC7440861.

870 11. Edenfield RC, Easley CAt. Implications of testicular ACE2 and the renin-angiotensin
871 system for SARS-CoV-2 on testis function. Nat Rev Urol. 2022;19(2):116-27. Epub 20211126.
872 doi: 10.1038/s41585-021-00542-5. PubMed PMID: 34837081; PMCID: PMC8622117.
873 12. Collins AB, Zhao L, Zhu Z, Givens NT, Bai Q, Wakefield MR, Fang Y. Impact of COVID-19
874 on Male Fertility. Urology. 2022. doi: 10.1016/J.UROLOGY.2021.12.025.
875 13. Parker AM, Brigham E, Connolly B, McPeake J, Agranovich AV, Kenes MT, Casey K,
876 Reynolds C, Schmidt KFR, Kim SY, Kaplin A, Sevin CM, Brodsky MB, Turnbull AE. Addressing the
877 post-acute sequelae of SARS-CoV-2 infection: a multidisciplinary model of care. Lancet Respir
878 Med. 2021;9(11):1328-41. Epub 20211019. doi: 10.1016/S2213-2600(21)00385-4. PubMed
879 PMID: 34678213; PMCID: PMC8525917.
880 14. Zhao JM, Zhou GD, Sun YL, Wang SS, Yang JF, Meng EH, Pan D, Li WS, Zhou XS, Wang YD,
881 Lu JY, Li N, Wang DW, Zhou BC, Zhang TH. [Clinical pathology and pathogenesis of severe acute
882 respiratory syndrome]. Zhonghua Shi Yan He Lin Chuang Bing Du Xue Za Zhi. 2003;17(3):217-21.
883 PubMed PMID: 15340561.
884 15. Xu J, Qi L, Chi X, Yang J, Wei X, Gong E, Peh S, Gu J. Orchitis: a complication of severe
885 acute respiratory syndrome (SARS). Biol Reprod. 2006;74(2):410-6. Epub 20051019. doi:
886 10.1095/biolreprod.105.044776. PubMed PMID: 16237152; PMCID: PMC7109827.
887 16. Beddingfield BJ, Maness NJ, Fears AC, Rappaport J, Aye PP, Russell-Lodrigue K, Doyle-
888 Meyers LA, Blair RV, Carias AM, Madden PJ, Redondo RL, Gao H, Montefiori D, Hope TJ, Roy CJ.
889 Effective prophylaxis of COVID-19 in rhesus macaques using a combination of two parentally-
890 administered SARS-CoV-2 neutralizing antibodies. bioRxiv. 2021:2021.05.26.445878-
891 2021.05.26. doi: 10.1101/2021.05.26.445878.
892 17. Blair RV, Vaccari M, Doyle-Meyers LA, Roy CJ, Russell-Lodrigue K, Fahlberg M, Monjure
893 CJ, Beddingfield B, Plante KS, Plante JA, Weaver SC, Qin X, Midkiff CC, Lehmicke G, Golden N,
894 Threeton B, Penney T, Allers C, Barnes MB, Pattison M, Datta PK, Maness NJ, Birnbaum A,
895 Fischer T, Bohm RP, Rappaport J. Acute Respiratory Distress in Aged, SARS-CoV-2–Infected
896 African Green Monkeys but Not Rhesus Macaques. The American Journal of Pathology.
897 2021;191(2):274-82. doi: 10.1016/J.AJPATH.2020.10.016.
898 18. Chandrashekar A, Liu J, Martino AJ, McMahan K, Mercad NB, Peter L, Tostanosk LH, Yu J,
899 Maliga Z, Nekorchuk M, Busman-Sahay K, Terry M, Wriji LM, Ducat S, Martine DR, Atyeo C,
900 Fischinger S, Burk JS, Slei MD, Pessaint L, Van Ry A, Greenhouse J, Taylor T, Blade K, Cook A,
901 Finneyfrock B, Brown R, Teow E, Velasco J, Zahn R, Wegmann F, Abbink P, Bondzi EA, Dagotto
902 G, Gebr MS, He X, Jacob-Dolan C, Kordana N, Li Z, Lifto MA, Mahrokhia SH, Maxfiel LF,
903 Nityanandam R, Nkolol JP, Schmid AG, Mille AD, Bari RS, Alter G, Sorge PK, Este JD, Andersen H,
904 Lewi MG, Barou DH. SARS-CoV-2 infection protects against rechallenge in rhesus macaques.
905 Science. 2020;369(6505):812-7. doi: 10.1126/SCIENCE.ABC4776.
906 19. Fahlberg MD, Blair RV, Doyle-Meyers LA, Midkiff CC, Zenere G, Russell-Lodrigue KE,
907 Monjure CJ, Haupt EH, Penney TP, Lehmicke G, Threeton BM, Golden N, Datta PK, Roy CJ, Bohm
908 RP, Maness NJ, Fischer T, Rappaport J, Vaccari M. Cellular events of acute, resolving or
909 progressive COVID-19 in SARS-CoV-2 infected non-human primates. Nat Commun.
910 2020;11(1):6078. Epub 20201127. doi: 10.1038/s41467-020-19967-4. PubMed PMID:
911 33247138; PMCID: PMC7695721.
912 20. Blair RV, Vaccari M, Doyle-Meyers LA, Roy CJ, Russell-Lodrigue K, Fahlberg M, Monjure
913 CJ, Beddingfield B, Plante KS, Plante JA, Weaver SC, Qin X, Midkiff CC, Lehmicke G, Golden N,

914 Threeton B, Penney T, Allers C, Barnes MB, Pattison M, Datta PK, Maness NJ, Birnbaum A,
915 Fischer T, Bohm RP, Rappaport J. Acute Respiratory Distress in Aged, SARS-CoV-2-Infected
916 African Green Monkeys but Not Rhesus Macaques. Am J Pathol. 2021;191(2):274-82. Epub
917 20201107. doi: 10.1016/j.ajpath.2020.10.016. PubMed PMID: 33171111; PMCID: PMC7648506.
918 21. Santangelo PJ, Rogers KA, Zurla C, Blanchard EL, Gumber S, Strait K, Connor-Stroud F,
919 Schuster DM, Amancha PK, Hong JJ, Byrareddy SN, Hoxie JA, Vidakovic B, Ansari AA, Hunter E,
920 Villinger F. Whole-body immunoPET reveals active SIV dynamics in viremic and antiretroviral
921 therapy-treated macaques. Nat Methods. 2015;12(5):427-32. Epub 2015/03/10. doi:
922 10.1038/nmeth.3320. PubMed PMID: 25751144; PMCID: PMC4425449.
923 22. Taylor RA, McRaven MD, Carias AM, Anderson MR, Matias E, Arainga M, Allen EJ, Rogers
924 KA, Gupta S, Kulkarni V, Lakhashe S, Lorenzo-Redondo R, Thomas Y, Strickland A, Villinger FJ,
925 Ruprecht RM, Hope TJ. Localization of infection in neonatal rhesus macaques after oral viral
926 challenge. PLoS Pathog. 2021;17(11):e1009855. Epub 20211118. doi:
927 10.1371/journal.ppat.1009855. PubMed PMID: 34793582; PMCID: PMC8639050.
928 23. Taylor RA, Xiao S, Carias AM, McRaven MD, Thakkar DN, Arainga M, Allen EJ, Rogers KA,
929 Kumarapperuma SC, Gong S, Fought AJ, Anderson MR, Thomas Y, Schneider JR, Goins B, Fox P,
930 Villinger FJ, Ruprecht RM, Hope TJ. PET/CT targeted tissue sampling reveals virus specific dIgA
931 can alter the distribution and localization of HIV after rectal exposure. PLoS Pathog.
932 2021;17(6):e1009632. Epub 20210601. doi: 10.1371/journal.ppat.1009632. PubMed PMID:
933 34061907; PMCID: PMC8195437.
934 24. Madden PJ, Arif MS, Becker ME, McRaven MD, Carias AM, Lorenzo-Redondo R, Xiao S,
935 Midkiff CC, Blair RV, Potter EL, Martin-Sancho L, Dodson A, Martinelli E, Todd JM, Villinger FJ,
936 Chanda SK, Aye PP, Roy CJ, Roederer M, Lewis MG, Veazey RS, Hope TJ. Development of an In
937 Vivo Probe to Track SARS-CoV-2 Infection in Rhesus Macaques. Front Immunol.
938 2021;12:810047. Epub 20211224. doi: 10.3389/fimmu.2021.810047. PubMed PMID: 35003140;
939 PMCID: PMC8739270.
940 25. Fahlberg MD, Blair RV, Doyle-Meyers LA, Midkiff CC, Zenere G, Russell-Lodrigue KE,
941 Monjure CJ, Haupt EH, Penney TP, Lehmicke G, Threeton BM, Golden N, Datta PK, Roy CJ, Bohm
942 RP, Maness NJ, Fischer T, Rappaport J, Vaccari M. Cellular events of acute, resolving or
943 progressive COVID-19 in SARS-CoV-2 infected non-human primates. Nature Communications
944 2020 11:1. 2020;11(1):1-14. doi: 10.1038/s41467-020-19967-4.
945 26. Gao G, Hu X, Zhou Y, Rao J, Zhang X, Peng Y, Zhao J, Yao Y, Liu K, Liang M, Liu H, Deng F,
946 Xia H, Shan C, Yuan Z. Infection and pathogenesis of the Delta variant of SARS-CoV-2 in Rhesus
947 macaque. Virologica Sinica. 2022. doi: 10.1016/j.virs.2022.02.001.
948 27. Nicolas N, Michel V, Bhushan S, Wahle E, Hayward S, Ludlow H, de Kretser DM, Loveland
949 KL, Schuppe HC, Meinhardt A, Hedger MP, Fijak M. Testicular activin and follistatin levels are
950 elevated during the course of experimental autoimmune epididymo-orchitis in mice. Sci Rep.
951 2017;7:42391. Epub 20170213. doi: 10.1038/srep42391. PubMed PMID: 28205525; PMCID:
952 PMC5304336.
953 28. Cardona-Maya W, Velilla PA, Montoya CJ, Cadavid A, Rugeles MT. In vitro human
954 immunodeficiency virus and sperm cell interaction mediated by the mannose receptor. J
955 Reprod Immunol. 2011;92(1-2):1-7. Epub 20111019. doi: 10.1016/j.jri.2011.09.002. PubMed
956 PMID: 22015004.

957 29. Cardona-Maya W, Lopez-Herrera A, Velilla-Hernandez P, Rugeles MT, Cadavid AP. The
958 role of mannose receptor on HIV-1 entry into human spermatozoa. Am J Reprod Immunol.
959 2006;55(4):241-5. doi: 10.1111/j.1600-0897.2005.00340.x. PubMed PMID: 16533334.
960 30. Benoff S, Hurley I, Cooper GW, Mandel FS, Hershlag A, Scholl GM, Rosenfeld DL.
961 Fertilization potential in vitro is correlated with head-specific mannose-ligand receptor
962 expression, acrosome status and membrane cholesterol content. Hum Reprod.
963 1993;8(12):2155-66. doi: 10.1093/oxfordjournals.humrep.a137997. PubMed PMID: 8150918.
964 31. Corbett KS, Flynn B, Foulds KE, Francica JR, Boyoglu-Barnum S, Werner AP, Flach B,
965 O'Connell S, Bock KW, Minai M, Nagata BM, Andersen H, Martinez DR, Noe AT, Douek N,
966 Donaldson MM, Nji NN, Alvarado GS, Edwards DK, Flebbe DR, Lamb E, Doria-Rose NA, Lin BC,
967 Louder MK, O'Dell S, Schmidt SD, Phung E, Chang LA, Yap C, Todd J-PM, Pessaint L, Ry AV,
968 Browne S, Greenhouse J, Putman-Taylor T, Strasbaugh A, Campbell T-A, Cook A, Dodson A,
969 Steingrebe K, Shi W, Zhang Y, Abiona OM, Wang L, Pegu A, Yang ES, Leung K, Zhou T, Teng IT,
970 Widge A, Gordon I, Novik L, Gillespie RA, Loomis RJ, Moliva JI, Stewart-Jones G, Himansu S, Kong
971 W-P, Nason MC, Morabito KM, Ruckwardt TJ, Ledgerwood JE, Gaudinski MR, Kwong PD,
972 Mascola JR, Carfi A, Lewis MG, Baric RS, McDermott A, Moore IN, Sullivan NJ, Roederer M,
973 Seder RA, Graham BS. Evaluation of the mRNA-1273 Vaccine against SARS-CoV-2 in Nonhuman
974 Primates. https://doiorg/101056/NEJMoa2024671. 2020;383(16):1544-55. doi:
975 10.1056/NEJMOA2024671.
976 32. Lindsay KE, Bhosle SM, Zurla C, Beyersdorf J, Rogers KA, Vanover D, Xiao P, Araínga M,
977 Shirreff LM, Pitard B, Baumhof P, Villinger F, Santangelo PJ. Visualization of early events in
978 mRNA vaccine delivery in non-human primates via PET–CT and near-infrared imaging. Nature
979 Biomedical Engineering 2019 3:5. 2019;3(5):371-80. doi: 10.1038/s41551-019-0378-3.
980 33. Soriano JB, Murthy S, Marshall JC, Relan P, Diaz JV, Condition WHOCCDWGoP-C-. A
981 clinical case definition of post-COVID-19 condition by a Delphi consensus. Lancet Infect Dis.
982 2021. Epub 20211221. doi: 10.1016/S1473-3099(21)00703-9. PubMed PMID: 34951953;
983 PMCID: PMC8691845.
984 34. Ward H, Flower B, Garcia PJ, Ong SWX, Altmann DM, Delaney B, Smith N, Elliott P, Cooke
985 G. Global surveillance, research, and collaboration needed to improve understanding and
986 management of long COVID. Lancet. 2021;398(10316):2057-9. Epub 20211110. doi:
987 10.1016/S0140-6736(21)02444-2. PubMed PMID: 34774190; PMCID: PMC8580495.
988 35. Duarte-Neto AN, Teixeira TA, Caldini EG, Kanamura CT, Gomes-Gouvea MS, Dos Santos
989 ABG, Monteiro RAA, Pinho JRR, Mauad T, da Silva LFF, Saldiva PHN, Dolhnikoff M, Leite KRM,
990 Hallak J. Testicular pathology in fatal COVID-19: A descriptive autopsy study. Andrology.
991 2022;10(1):13-23. Epub 20210716. doi: 10.1111/andr.13073. PubMed PMID: 34196475; PMCID:
992 PMC8444746.
993 36. Moghimi N, Eslami Farsani B, Ghadipasha M, Mahmoudiasl GR, Piryaei A, Aliaghaei A,
994 Abdi S, Abbaszadeh HA, Abdollahifar MA, Forozesh M. COVID-19 disrupts spermatogenesis
995 through the oxidative stress pathway following induction of apoptosis. Apoptosis. 2021;26(7-
996 8):415-30. Epub 20210602. doi: 10.1007/s10495-021-01680-2. PubMed PMID: 34076792;
997 PMCID: PMC8170653.
998 37. Yang M, Chen S, Huang B, Zhong JM, Su H, Chen YJ, Cao Q, Ma L, He J, Li XF, Li X, Zhou JJ,
999 Fan J, Luo DJ, Chang XN, Arkun K, Zhou M, Nie X. Pathological Findings in the Testes of COVID-

1000 19 Patients: Clinical Implications. Eur Urol Focus. 2020;6(5):1124-9. Epub 20200531. doi:
1001 10.1016/j.euf.2020.05.009. PubMed PMID: 32563676; PMCID: PMC7261470.
1002 38. Peirouvi T, Aliaghaei A, Eslami Farsani B, Ziaeipour S, Ebrahimi V, Forozesh M,
1003 Ghadipasha M, Mahmoudiasl GR, Aryan A, Moghimi N, Abdi S, Raoofi A, Kargar Godaneh M,
1004 Abdollahifar MA. COVID-19 disrupts the blood-testis barrier through the induction of
1005 inflammatory cytokines and disruption of junctional proteins. Inflamm Res. 2021;70(10-
1006 12):1165-75. Epub 20210826. doi: 10.1007/s00011-021-01497-4. PubMed PMID: 34436630;
1007 PMCID: PMC8387554.
1008 39. Achua JK, Chu KY, Ibrahim E, Khodamoradi K, Delma KS, Iakymenko OA, Kryvenko ON,
1009 Arora H, Ramasamy R. Histopathology and Ultrastructural Findings of Fatal COVID-19 Infections
1010 on Testis. World J Mens Health. 2021;39(1):65-74. Epub 20201103. doi: 10.5534/wjmh.200170.
1011 PubMed PMID: 33151050; PMCID: PMC7752514.
1012 40. Ma X, Guan C, Chen R, Wang Y, Feng S, Wang R, Qu G, Zhao S, Wang F, Wang X, Zhang D,
1013 Liu L, Liao A, Yuan S. Pathological and molecular examinations of postmortem testis biopsies
1014 reveal SARS-CoV-2 infection in the testis and spermatogenesis damage in COVID-19 patients.
1015 Cellular and Molecular Immunology. 2021;18(2):487-9. doi: 10.1038/s41423-020-00604-5.
1016 41. Ardestani Zadeh A, Arab D. COVID-19 and male reproductive system: pathogenic
1017 features and possible mechanisms. J Mol Histol. 2021;52(5):869-78. Epub 20210707. doi:
1018 10.1007/s10735-021-10003-3. PubMed PMID: 34232425; PMCID: PMC8260577.
1019 42. Liu X, Chen Y, Tang W, Zhang L, Chen W, Yan Z, Yuan P, Yang M, Kong S, Yan L, Qiao J.
1020 Single-cell transcriptome analysis of the novel coronavirus (SARS-CoV-2) associated gene ACE2
1021 expression in normal and non-obstructive azoospermia (NOA) human male testes. Sci China Life
1022 Sci. 2020;63(7):1006-15. Epub 20200430. doi: 10.1007/s11427-020-1705-0. PubMed PMID:
1023 32361911; PMCID: PMC7195615.
1024 43. Li X, Lu H, Li F, Zhang Q, Wang T, Qiang L, Yang Q. Impacts of COVID-19 and SARS-CoV-2
1025 on male reproductive function: a systematic review and meta-analysis protocol. BMJ Open.
1026 2022;12(1):e053051. Epub 20220105. doi: 10.1136/bmjopen-2021-053051. PubMed PMID:
1027 34987042.
1028 44. Li C, Ye Z, Zhang AJ, Chan JF, Song W, Liu F, Chen Y, Kwan MY, Lee AC, Zhao Y, Wong BH,
1029 Yip CC, Cai JP, Lung DC, Sridhar S, Jin D, Chu H, To KK, Yuen KY. Severe acute respiratory
1030 syndrome coronavirus 2 (SARS-CoV-2) infections by intranasal or testicular inoculation induces
1031 testicular damage preventable by vaccination in golden Syrian hamsters. Clin Infect Dis. 2022.
1032 Epub 20220218. doi: 10.1093/cid/ciac142. PubMed PMID: 35178548.
1033 45. Campos RK, Camargos VN, Azar SR, Haines CA, Eyzaguirre EJ, Rossi SL. SARS-CoV-2
1034 Infects Hamster Testes. Microorganisms. 2021;9(6). Epub 20210617. doi:
1035 10.3390/microorganisms9061318. PubMed PMID: 34204370; PMCID: PMC8235703.
1036 46. Ullah I, Prevost J, Ladinsky MS, Stone H, Lu M, Anand SP, Beaudoin-Bussieres G, Symmes
1037 K, Benlarbi M, Ding S, Gasser R, Fink C, Chen Y, Tauzin A, Goyette G, Bourassa C, Medjahed H,
1038 Mack M, Chung K, Wilen CB, Dekaban GA, Dikeakos JD, Bruce EA, Kaufmann DE, Stamatatos L,
1039 McGuire AT, Richard J, Pazgier M, Bjorkman PJ, Mothes W, Finzi A, Kumar P, Uchil PD. Live
1040 imaging of SARS-CoV-2 infection in mice reveals that neutralizing antibodies require Fc function
1041 for optimal efficacy. Immunity. 2021;54(9):2143-58 e15. Epub 20210818. doi:
1042 10.1016/j.immuni.2021.08.015. PubMed PMID: 34453881; PMCID: PMC8372518.

1043 47. Pike JFW, Polley EL, Pritchett DY, Lal A, Wynia BA, Roudebush WE, Chosed RJ.
1044 Comparative analysis of viral infection outcomes in human seminal fluid from prior viral
1045 epidemics and Sars-CoV-2 may offer trends for viral sexual transmissibility and long-term
1046 reproductive health implications. Reprod Health. 2021;18(1):123. Epub 20210610. doi:
1047 10.1186/s12978-021-01172-1. PubMed PMID: 34112171; PMCID: PMC8192109.
1048 48. Massarotti C, Garolla A, Maccarini E, Scaruffi P, Stigliani S, Anserini P, Foresta C. SARS-
1049 CoV-2 in the semen: Where does it come from? Andrology. 2021;9(1):39-41. Epub 20200728.
1050 doi: 10.1111/andr.12839. PubMed PMID: 32533891; PMCID: PMC7323151.
1051 49. Haghpanah A, Masjedi F, Salehipour M, Hosseinpour A, Roozbeh J, Dehghani A. Is
1052 COVID-19 a risk factor for progression of benign prostatic hyperplasia and exacerbation of its
1053 related symptoms?: a systematic review. Prostate Cancer Prostatic Dis. 2021. Epub 20210518.
1054 doi: 10.1038/s41391-021-00388-3. PubMed PMID: 34007019; PMCID: PMC8129694.
1055 50. Stopsack KH, Mucci LA, Antonarakis ES, Nelson PS, Kantoff PW. TMPRSS2 and COVID-19:
1056 Serendipity or Opportunity for Intervention? Cancer Discov. 2020;10(6):779-82. Epub
1057 20200410. doi: 10.1158/2159-8290.CD-20-0451. PubMed PMID: 32276929; PMCID:
1058 PMC7437472.
1059 51. Gedeborg R, Styrke J, Loeb S, Garmo H, Stattin P. Androgen deprivation therapy and
1060 excess mortality in men with prostate cancer during the initial phase of the COVID-19
1061 pandemic. PLoS One. 2021;16(10):e0255966. Epub 20211007. doi:
1062 10.1371/journal.pone.0255966. PubMed PMID: 34618806; PMCID: PMC8496782.
1063 52. Soumarova R, Boday A, Krhutova V, Janotova A, Dvorakova M, Jaluvkova E, Stursa M,
1064 Perkova H. Prognostic and predictive molecular biological markers in prostate cancer -
1065 significance of expression of genes PCA3 and TMPRSS2. Neoplasma. 2015;62(1):114-8. doi:
1066 10.4149/neo_2015_014. PubMed PMID: 25563374.
1067 53. Bhowmick NA, Oft J, Dorff T, Pal S, Agarwal N, Figlin RA, Posadas EM, Freedland SJ, Gong
1068 J. COVID-19 and androgen-targeted therapy for prostate cancer patients. Endocr Relat Cancer.
1069 2020;27(9):R281-R92. doi: 10.1530/ERC-20-0165. PubMed PMID: 32508311; PMCID:
1070 PMC7546583.
1071 54. Kazan O, Culpan M, Efiloglu O, Atis G, Yildirim A. The clinical impact of androgen
1072 deprivation therapy on SARS-CoV-2 infection rates and disease severity. Turk J Urol.
1073 2021;47(6):495-500. doi: 10.5152/tud.2021.21278. PubMed PMID: 35118968.
1074 55. Cinislioglu AE, Demirdogen SO, Cinislioglu N, Altay MS, Sam E, Akkas F, Tor IH, Aydin HR,
1075 Karabulut I, Ozbey I. Variation of Serum PSA Levels in COVID-19 Infected Male Patients with
1076 Benign Prostatic Hyperplasia (BPH): A Prospective Cohort Studys. Urology. 2022;159:16-21.
1077 Epub 20211006. doi: 10.1016/j.urology.2021.09.016. PubMed PMID: 34626600; PMCID:
1078 PMC8493783.
1079 56. Mohamed MS, Moulin TC, Schioth HB. Sex differences in COVID-19: the role of
1080 androgens in disease severity and progression. Endocrine. 2021;71(1):3-8. Epub 20201111. doi:
1081 10.1007/s12020-020-02536-6. PubMed PMID: 33179220; PMCID: PMC7657570.
1082 57. Reddy R, Farber N, Kresch E, Seetharam D, Diaz P, Ramasamy R. SARS-CoV-2 in the
1083 Prostate: Immunohistochemical and Ultrastructural Studies. The World Journal of Men's Health.
1084 2021;40. doi: 10.5534/WJMH.210174.
1085 58. Fraga-Silva RA, Costa-Fraga FP, Montecucco F, Sturny M, Faye Y, Mach F, Pelli G, Shenoy
1086 V, da Silva RF, Raizada MK, Santos RA, Stergiopulos N. Diminazene protects corpus cavernosum

1087 against hypercholesterolemia-induced injury. J Sex Med. 2015;12(2):289-302. Epub 20141120.
1088 doi: 10.1111/jsm.12757. PubMed PMID: 25411084.
1089 59. Kresch E, Achua J, Saltzman R, Khodamoradi K, Arora H, Ibrahim E, Kryvenko ON, Wolff
1090 Almeida V, Firdaus F, Hare JM, Ramasamy R. COVID-19 Endothelial Dysfunction Can Cause
1091 Erectile Dysfunction: Histopathological, Immunohistochemical, and Ultrastructural Study of the
1092 Human Penis. World J Mens Health. 2021;39:2287-4208. doi: 10.5534/wjmh.210055.
1093 60. Sansone A, Mollaioli D, Ciocca G, Colonnello E, Limoncin E, Balercia G, Jannini EA. "Mask
1094 up to keep it up": Preliminary evidence of the association between erectile dysfunction and
1095 COVID-19. Andrology. 2021;00:1-7. doi: 10.1111/andr.13003.
1096 61. Dal Moro F, Vendramin I, Livi U. The war against the SARS-CoV2 infection: Is it better to
1097 fight or mitigate it? Med Hypotheses. 2020;143:110129. Epub 20200722. doi:
1098 10.1016/j.mehy.2020.110129. PubMed PMID: 32721814; PMCID: PMC7373683.
1099 62. Mejri R, Mrad Dali K, Chaker K, Bibi M, Ben Rhouma S, Nouira Y. Venous thrombosis of
1100 the pampiniform plexus after coronavirus infection (COVID-19): A case report. Urol Case Rep.
1101 2021;39:101860. Epub 20210927. doi: 10.1016/j.eucr.2021.101860. PubMed PMID: 34603969;
1102 PMCID: PMC8475016.
1103 63. Alshoabi SA, Haider KH, Mostafa MA, Hamid AM, Daqqaq TS. An unusual and atypical
1104 presentation of the novel coronavirus: A case report and brief review of the literature. J Taibah
1105 Univ Med Sci. 2021;16(4):637-42. Epub 20210412. doi: 10.1016/j.jtumed.2021.01.014. PubMed
1106 PMID: 33867909; PMCID: PMC8038890.
1107 64. Whiteley MS, Abu-Bakr O, Holdstock JM. Testicular vein thrombosis mimicking
1108 epididymo-orchitis after suspected Covid-19 infection. SAGE Open Med Case Rep.
1109 2021;9:2050313X211022425. Epub 20210604. doi: 10.1177/2050313X211022425. PubMed
1110 PMID: 34158948; PMCID: PMC8182169.
1111 65. La Marca A, Busani S, Donno V, Guaraldi G, Ligabue G, Girardis M. Testicular pain as an
1112 unusual presentation of COVID-19: a brief review of SARS-CoV-2 and the testis. Reprod Biomed
1113 Online. 2020;41(5):903-6. Epub 20200723. doi: 10.1016/j.rbmo.2020.07.017. PubMed PMID:
1114 32826162; PMCID: PMC7377719.
1115 66. Li K, Liu X, Huang Y, Liu X, Song Q, Wang R. Evaluation of testicular spermatogenic
1116 function by ultrasound elastography in patients with varicocele-associated infertility. Am J
1117 Transl Res. 2021;13(8):9136-42. Epub 20210815. PubMed PMID: 34540028; PMCID:
1118 PMC8430184.
1119 67. Mali WP, Arndt JW, Coolsaet BL, Kremer J, Oei HY. Haemodynamic aspects of left-sided
1120 varicocele and its association with so-called right-sided varicocele. Int J Androl. 1984;7(4):297-
1121 308. doi: 10.1111/j.1365-2605.1984.tb00787.x. PubMed PMID: 6096276.
1122 68. Aitken RJ. COVID-19 and human spermatozoa—Potential risks for infertility and sexual
1123 transmission? Andrology. 2021;9(1):48-52. doi: 10.1111/andr.12859.
1124 69. Gacci M, Coppi M, Baldi E, Sebastianelli A, Zaccaro C, Morselli S, Pecoraro A, Manera A,
1125 Nicoletti R, Liaci A, Bisegna C, Gemma L, Giancane S, Pollini S, Antonelli A, Lagi F, Marchiani S,
1126 Dabizzi S, Degl'Innocenti S, Annunziato F, Maggi M, Vignozzi L, Bartoloni A, Rossolini GM, Serni
1127 S. Semen impairment and occurrence of SARS-CoV-2 virus in semen after recovery from COVID-
1128 19. Human Reproduction. 2021;0(0):1-10. doi: 10.1093/humrep/deab026.

1129 70. Sengupta P, Leisegang K, Agarwal A. The impact of COVID-19 on the male reproductive
1130 tract and fertility: A systematic review. Arab J Urol. 2021;19(3):423-36. Epub 20210809. doi:
1131 10.1080/2090598X.2021.1955554. PubMed PMID: 34552795; PMCID: PMC8451696.
1132 71. Li H, Xiao X, Zhang J, Zafar MI, Wu C, Long Y, Lu W, Pan F, Meng T, Zhao K, Zhou L, Shen
1133 S, Liu L, Liu Q, Xiong C. Impaired spermatogenesis in COVID-19 patients. EClinicalMedicine.
1134 2020;28. doi: 10.1016/j.eclinm.2020.100604.
1135 72. Delli Muti N, Finocchi F, Tossetta G, Salvio G, Cutini M, Marzioni D, Balercia G. Could
1136 SARS-CoV-2 infection affect male fertility and sexuality? APMIS. 2022. Epub 20220203. doi:
1137 10.1111/apm.13210. PubMed PMID: 35114008.
1138 73. Wesselink AK, Hatch EE, Rothman KJ, Wang TR, Willis MD, Yland J, Crowe HM, Geller RJ,
1139 Willis SK, Perkins RB, Regan AK, Levinson J, Mikkelsen EM, Wise LA. A prospective cohort study
1140 of COVID-19 vaccination, SARS-CoV-2 infection, and fertility. Am J Epidemiol. 2022. Epub
1141 20220120. doi: 10.1093/aje/kwac011. PubMed PMID: 35051292; PMCID: PMC8807200.
1142 74. Xu J, Qi L, Chi X, Yang J, Wei X, Gong E, Peh S, Gu J. Orchitis: A Complication of Severe
1143 Acute Respiratory Syndrome (SARS). Biology of Reproduction. 2006;74(2):410-6. doi:
1144 10.1095/BIOLREPROD.105.044776.
1145 75. Delle Fave RF, Polisini G, Giglioni G, Parlavecchio A, Dell'Atti L, Galosi AB. COVID-19 and
1146 male fertility: Taking stock of one year after the outbreak began. Archivio Italiano di Urologia e
1147 Andrologia. 2021;93(1):115-9. doi: 10.4081/aiua.2021.1.115.
1148 76. Al-Kuraishy HM, Al-Gareeb AI, Faidah H, Alexiou A, Batiha GE. Testosterone in COVID-19:
1149 An Adversary Bane or Comrade Boon. Front Cell Infect Microbiol. 2021;11:666987. Epub
1150 20210908. doi: 10.3389/fcimb.2021.666987. PubMed PMID: 34568081; PMCID: PMC8455954.
1151 77. Haghpanah A, Masjedi F, Alborzi S, Hosseinpour A, Dehghani A, Malekmakan L, Roozbeh
1152 J. Potential mechanisms of SARS-CoV-2 action on male gonadal function and fertility: Current
1153 status and future prospects. Andrologia. 2021;53(1):e13883-e. doi: 10.1111/and.13883.
1154 78. Enikeev D, Taratkin M, Morozov A, Petov V, Korolev D, Shpikina A, Spivak L, Kharlamova
1155 S, Shchedrina I, Mestnikov O, Fiev D, Ganzha T, Geladze M, Mambetova A, Kogan E, Zharkov N,
1156 Demyashkin G, Shariat SF, Glybochko P. Prospective two-arm study of the testicular function in
1157 patients with COVID-19. Andrology. 2022. Epub 20220206. doi: 10.1111/andr.13159. PubMed
1158 PMID: 35124885.
1159

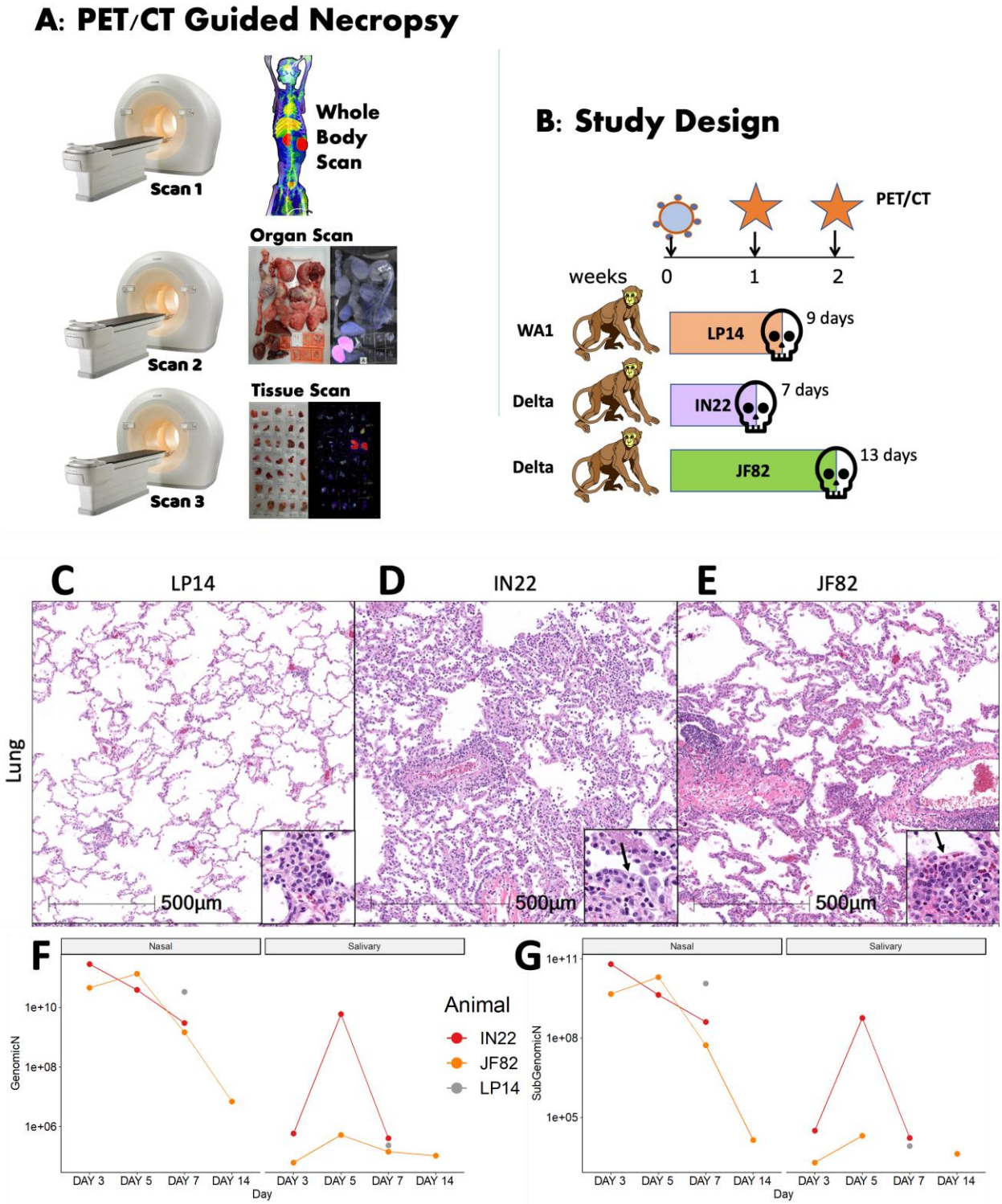

Figure 1. Study design and viral analysis of infected macaques. (A) Workflow of PET/CT guided necropsy. (B) Schematic showing the study design of probe administration, PET/CT scans, and infection. (C) (F and G) Viral load measurements for all three animals. (F) shows copies/swab of genomic N while (G) shows copies/swab of subgenomic N.

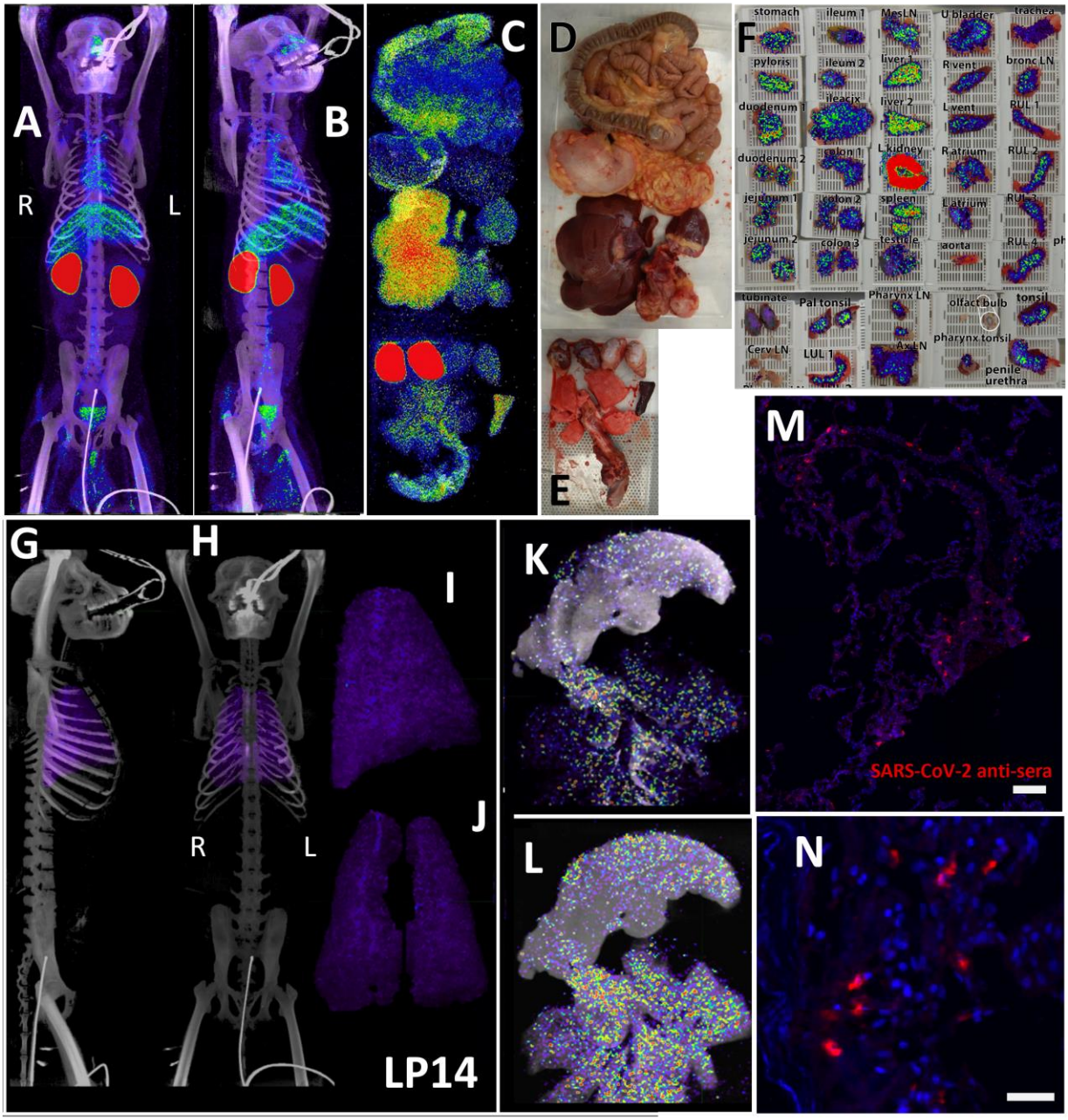

Figure 2. LP14 PET/CT guided necropsy. (A and B) Whole-body PET/CT scans of LP14 8 days post-infection. Front view (A) and rotated 45° (B) both shown. PET signal is display as SUV. (C) Post necropsy PET/CT organ scan of LP14. (D and E) Images of tissues scanned in (C). (F) Overlay of PET signal onto photograph of small pieces of tissue in cassettes. (G and H) Lung PET signal was isolated and overlaid on whole body CT scans. Side (G) and front (H) view. (I and J) Isolated lung PET volumes used in G and H are shown independently, side view (I) and front view (J). (K and L) Single axial z-slice images of respiratory tract PET/CT signals are shown, each image represents a single z-plane from scan shown in C. (M and N) Fluorescent microscopy images of LP14 lung tissue blocks. Red is SARS-CoV-2 anti-sera and blue is Hoechst nuclear stain. Scale bars 100 µM (M) and 25 µM (N).

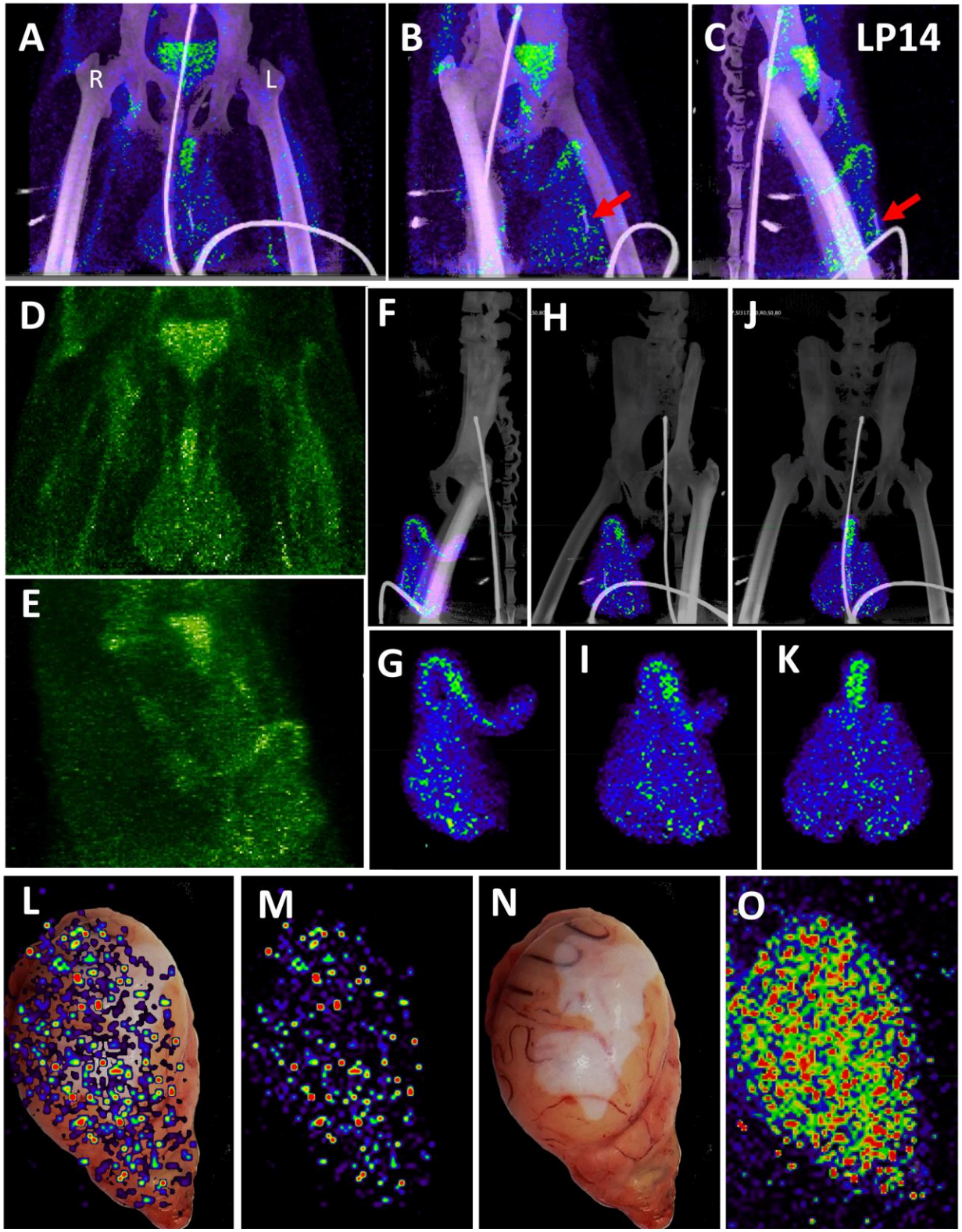
A
R
L
B
C
LP14
D
E
F
H
J
G
I
K
L
M
N
O

Figure 3. Male genital tract signal in LP14. (A, B, and C) PET/CT images highlighting the lower abdomen of LP14 from the whole-body scan. Front (A), rotated 45° (B), and side (C) views are all shown. Right and left labeled in front view. Red arrow in B and C shows location of baculum in CT scan. (D and E) PET signal with CT overlay removed to highlight signal in MGT, front (D) and side (E) views shown. (F, H, and J) Isolated 3D volume of MGT from whole body scan overlaid with CT images. Side (F), rotated 45° (H), and front (J) views shown. (G, I, and K) Isolated 3D volume of MGT used in overlays (F, H, and J) shown with same views. (L) Overlay of single z-plane of PET signal from organ scan onto image of testis of LP14. (M) PET signal from single z-plane of organ scan used in (L). (N) Image of LP14 testis used in (L). (O) 3D volume of PET signal from organ scan of single testis in previous panels.

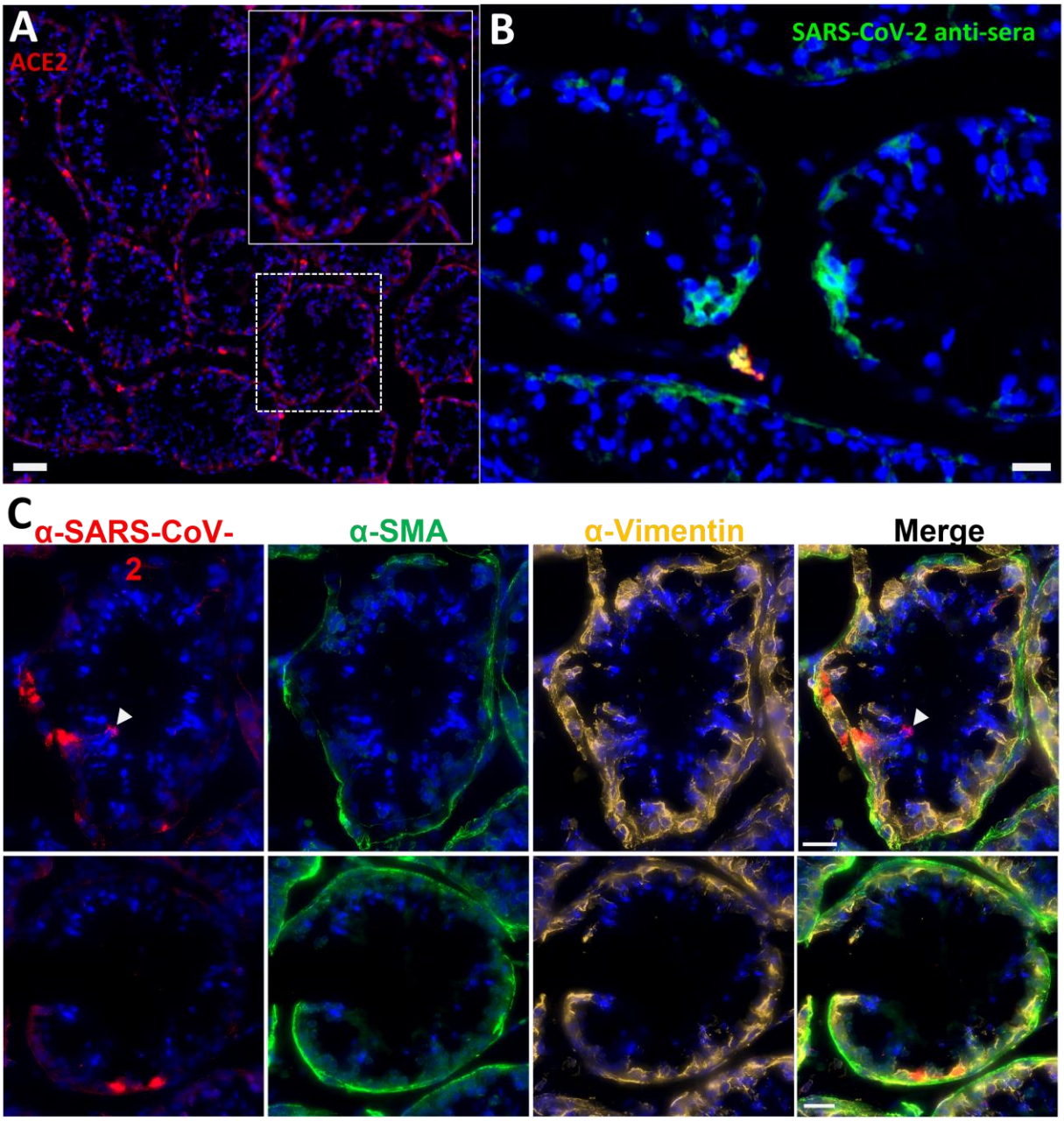

Figure 4. Immunofluorescence of LP14 Testes. (A) Fluorescent microscopy image of LP14 seminiferous tubules. ACE2 staining shown in red, Hoechst nuclear staining shown in blue. Inset shows zoom in of single tubule to better view ACE2 staining in Sertoli and myoid cells. Scale bars 50 µM. (B) Fluorescent microscopy image of LP14 testis shows infected cells. SARS-CoV-2 anti-sera staining in green, background fluorescent in red, and Hoechst nuclear staining in blue. Scale bars 25 µM. (C) Microscopy images of two tubules containing infected cells (top and bottom rows). Red is SARS-CoV-2 anti-sera, green is smooth muscle actin, gold is vimentin, and blue is Hoechst nuclear stain. Possible infected germ cells marked by arrow heads. Scale bars 20 µM.

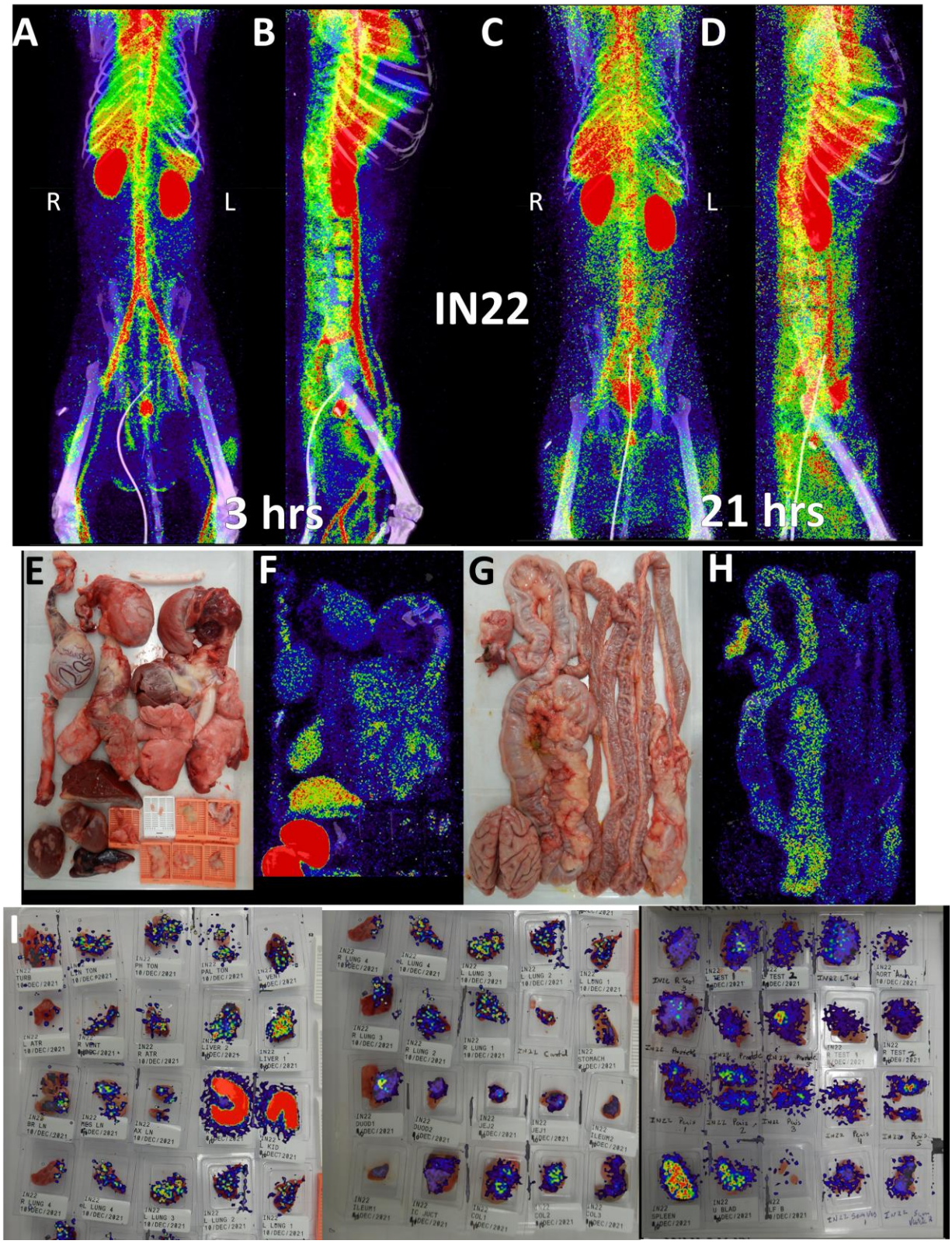
A
B
C
D
R
L
R
L
IN22
3 hrs
21 hrs
E
F
G
H
I

1206 **Figure 5. IN22 PET/CT guided necropsy images.** (A and B) Whole-body PET/CT scans of IN22
1207 obtained 3-hours after probe administration. Front view (A) and side (B) both shown. (C and D)
1208 Whole-body PET/CT scans of IN22 obtained 21-hours after probe administration. Front view (C)
1209 and side (D) both shown. Right and left labeled in front views (A and C). (E) Organ tray post
1210 necropsy and (F) PET/CT image. (G) Second organ tray post necropsy and (H) PET/CT image. (I)
1211 Overlay of PET signal onto photograph of tissue cassettes.
1212

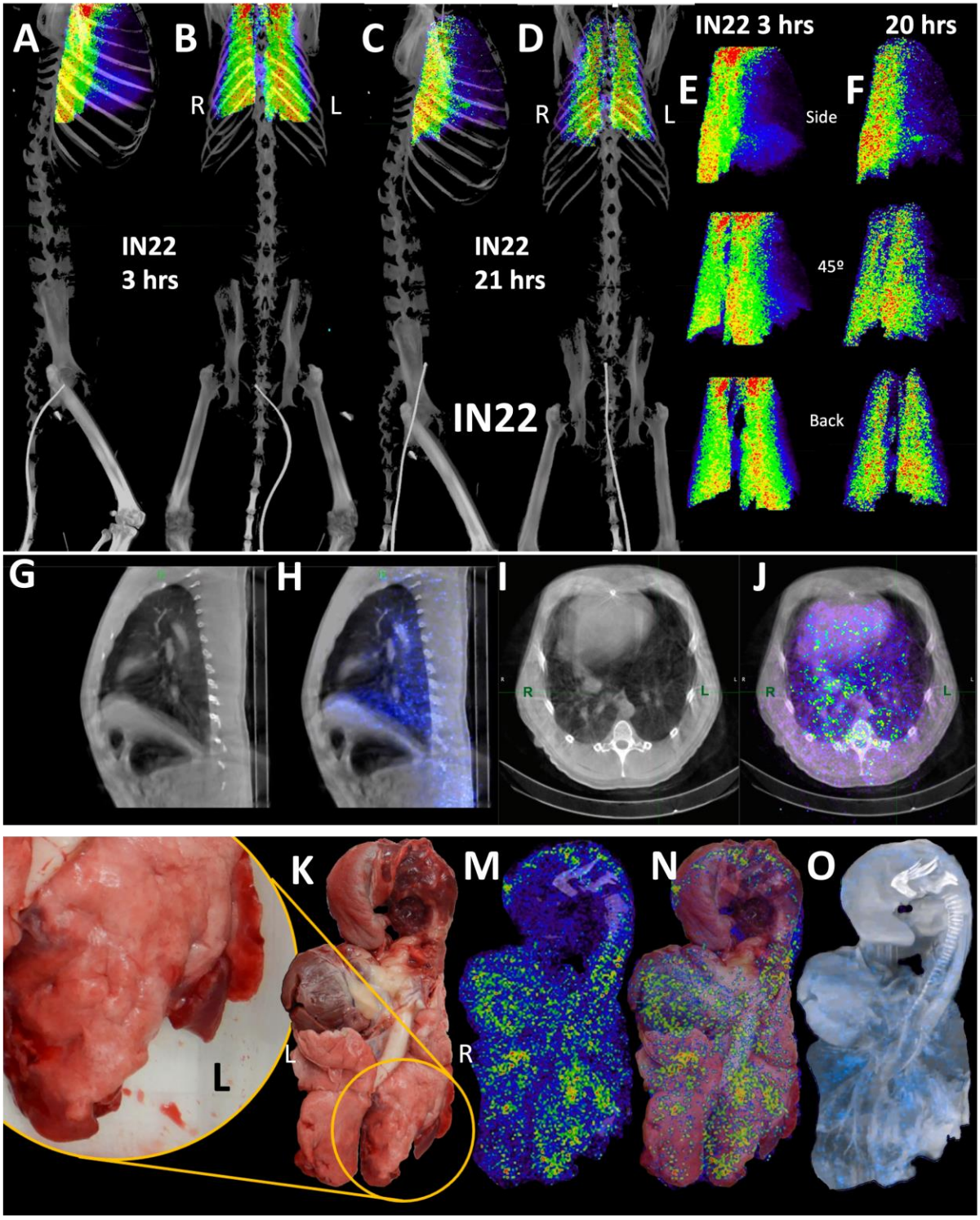
A
B
C
D
R
L
R
L
IN22 3 hrs
20 hrs
E
F
Side
IN22
3 hrs
IN22
21 hrs
45º
IN22
Back
G
H
I
J
R
L
R
L
K
M
N
O
L
L
R

1213

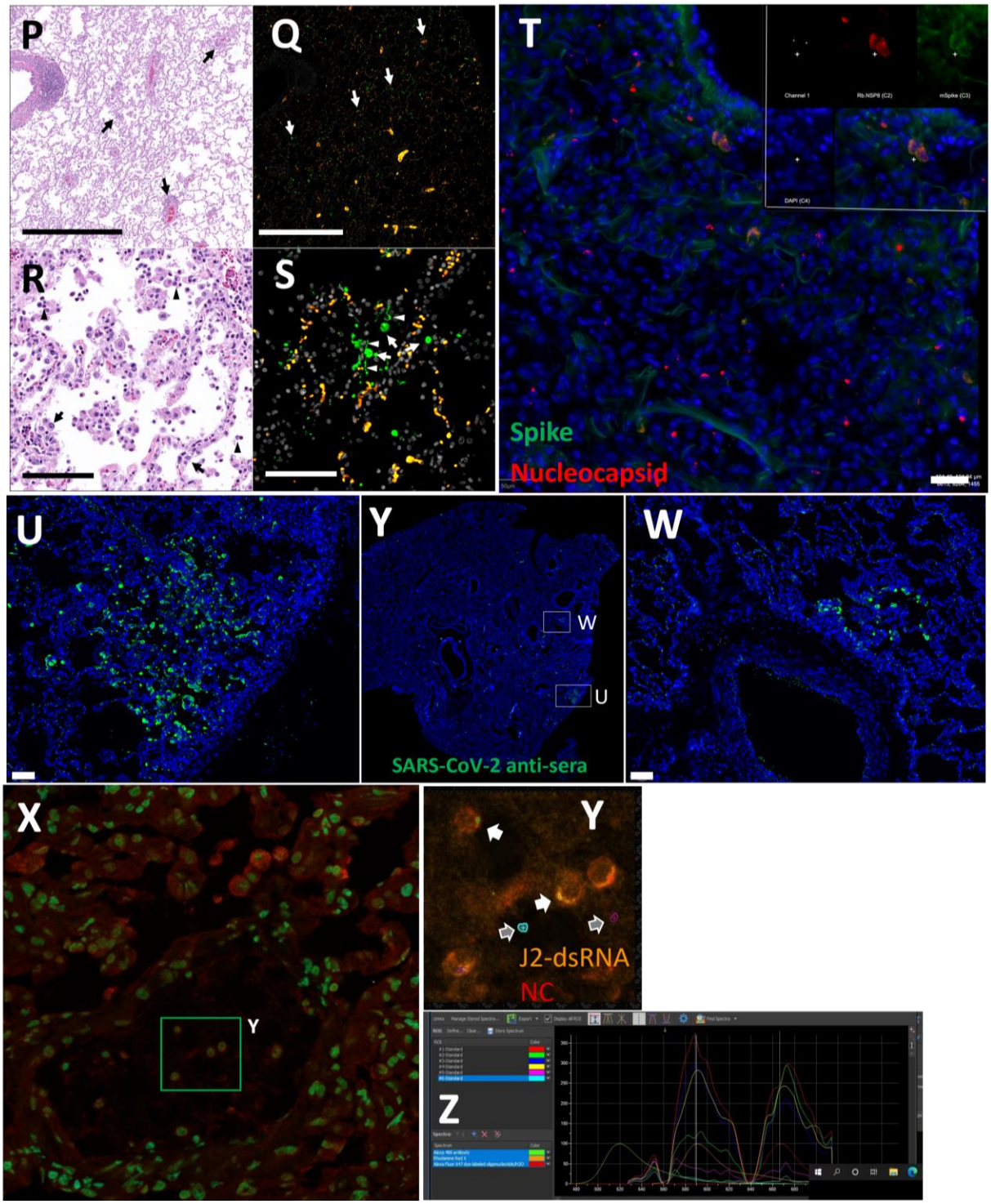

Figure 6. IN22 lung pathology and PET signal. (A-D) Lung PET volumes were isolated and overlaid on whole body CT scans. (A and B) Show lung volumes from 3-hour scan, side (A) and front (B) views shown. (C and D) Show lung volumes from 21-hour scan, side (C) and front (D) views shown. (E and F) Isolated lung PET volumes for each scan are shown independent of CT. (G) Sagittal z-slice from CT showing lungs. (H) PET signal overlaid on z-slice from G. (I)

1221 Transverse z-slice through torso from CT. (J) PET signal overlaid on z-slice from I. (K) Image of
1222 respiratory tract after necropsy. (L) Inset showing overt lung pathology in right lower lobe. (M)
1223 PET/CT signal from organ scan of respiratory tract. (N) PET/CT signal from M overlaid onto
1224 image from K. (O) PET/CT signal with CT contrast increased to observe pathology in lower right
1225 lung lobe. (P) H&E image of lung tissue showing areas of expanded alveolar space and
1226 inflammatory infiltrate (arrows). (Q) Immunofluorescence image of the same tissue from P.
1227 Green is SARS-CoV-2 anti-sera, red is background, and white is nuclear stain. White arrows
1228 indicate SARS-CoV-2 positive cells. (R) H&E image of lung tissue showing macrophages and
1229 neutrophils (arrowheads) and type II pneumocytes (arrows). (S) Immunofluorescence image
1230 showing infected cells of the alveoli (arrows) and lining the alveolar septa (arrowheads). Green
1231 is SARS-CoV-2 anti-sera, red is background, white is nuclear stain. All scale bars are 100 µM. (T)
1232 Fluorescent microscopy image of IN22 lung tissue. Spike shown in green, nucleocapsid shown in
1233 red, background in white, and Hoechst nuclear stain in blue. Scale bar 100 µM. (U, Y, W)
1234 Additional fluorescent microscopy images of lung tissue showing foci of infected cells. U and W
1235 are shown in low magnification Y. Green is SARS-CoV-2 anti-sera and blue is Hoechst nuclear
1236 stain. Scales bar 500 µM. (X-Z) Validation of dual antibody staining utilizing spectral imaging. (X)
1237 shows microscopy of J2 antibody with redX secondary and rabbit anti-NC monoclonal and Cy5
1238 secondary. (Y) Shows area within green square in X. White arrows point to regions of interest
1239 that are cell associated. Grey arrows indicate control regions of spectral evaluation. The areas
1240 evaluated by spectral imaging in (Y) are color coded and match with the spectra shown in (Z).

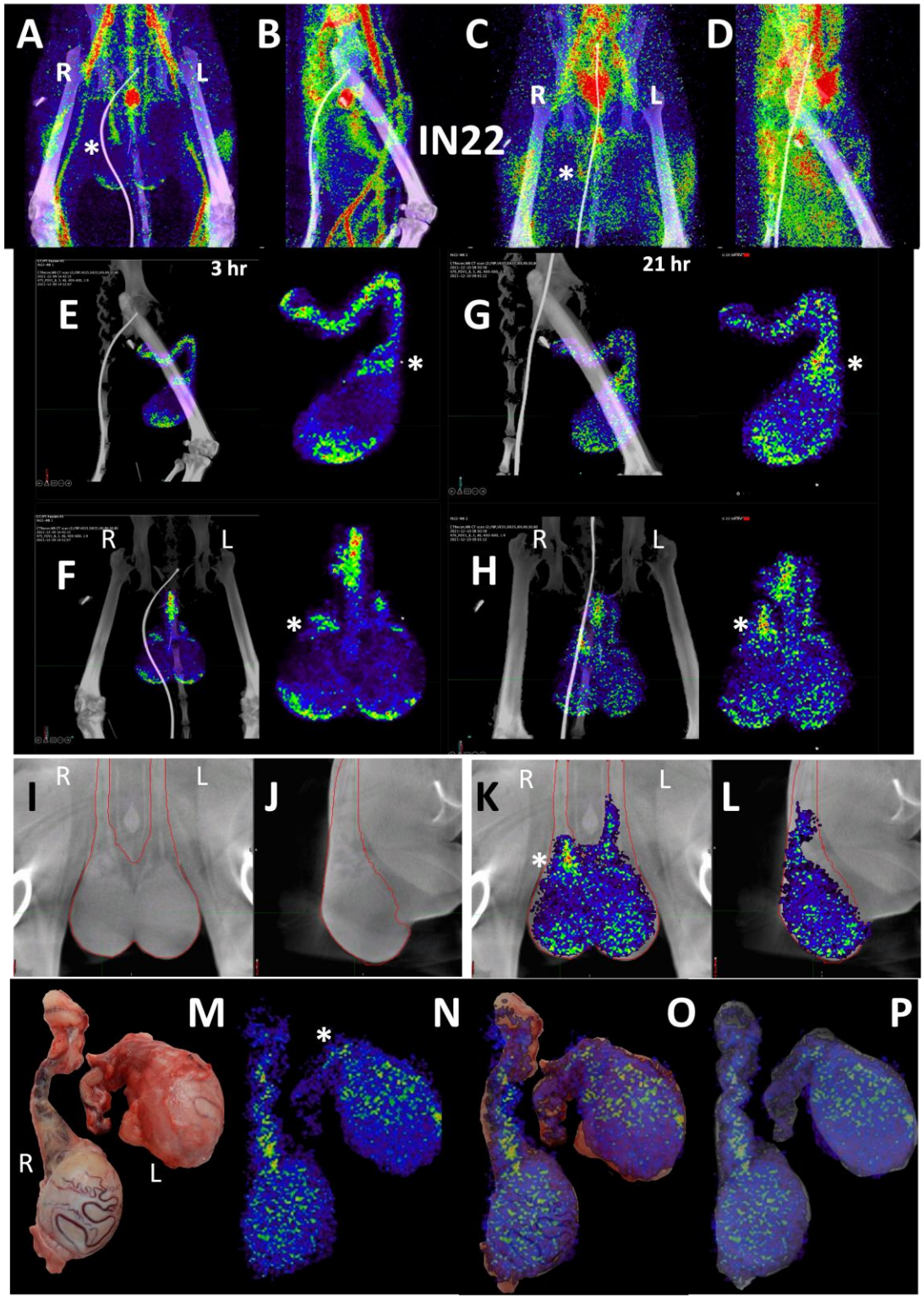

1241

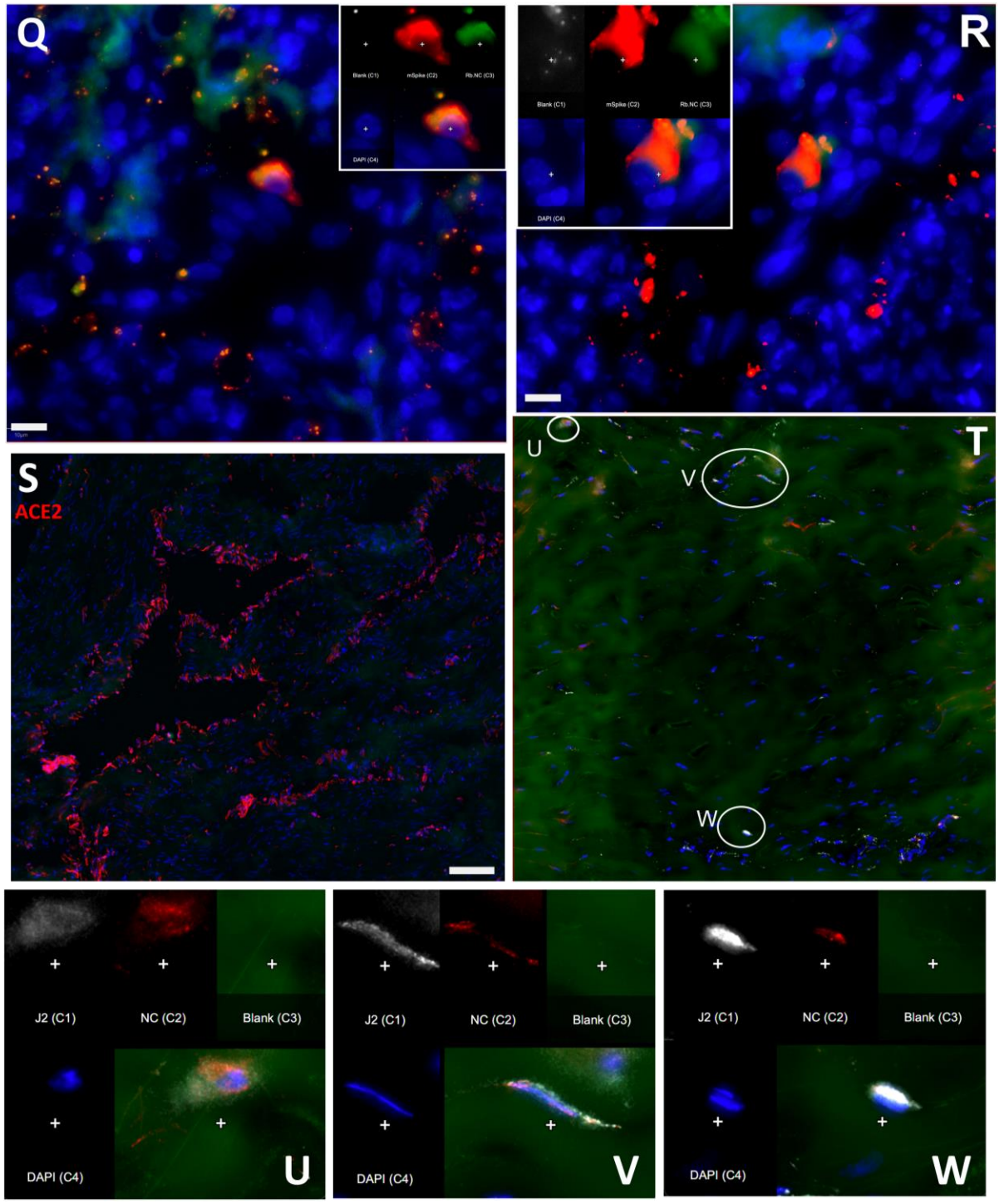

Figure 7. Male genital tract signal of IN22. (A and B) PET/CT images highlighting the lower abdomen of IN22 obtained 3-hours after probe administration. Front view (A) and side (B) both shown. (C and D) PET/CT images highlighting the lower abdomen of IN22 obtained 21-hours after probe administration. Front view (C) and side (D) both shown. (E and F) Isolated 3D volume of MGT from 3-hour scan overlaid with whole-body CT. Side (E) and front (F) views

1249 shown. (G and H) Isolated 3D volume of MGT from 21-hour scan overlaid with whole-body CT.
1250 Side (G) and front (H) views shown. (I and J) Whole-body CT images of lower abdomen, red
1251 contours outline the testicles and spermatic cords. Front (I) and side (J) views shown. (K and L)
1252 3D volume of MGT overlaid onto CT images from previous panels. (M) Image of testicles after
1253 necropsy. (N) PET signal from organ scan of testicles. (O) Overlay of PET signal onto image from
1254 panel M. (P) Overlay of PET signal onto CT signal from same scan. White asterisks mark location
1255 of pampiniform plexus in all previous panels. (Q and R) Fluorescence microscopy of SARS-CoV-2
1256 infected cells in testicular tissue from IN22. Red is SARS-CoV-2 spike, green is SARS-CoV-2
1257 nucleocapsid, white is background, and blue is Hoechst nuclear stain. Insets show channels
1258 independently, larger image is all channels merged. Scale bars 10 µM (S) Fluorescent
1259 microscopy image of corpus cavernosum tissue from an uninfected animal showing ACE2
1260 staining in red, background in green, and Hoechst nuclear staining in blue. Scale bar 100 µM (T)
1261 Fluorescence microscopy of SARS-CoV-2 infected cells in penile tissue from IN22. White is
1262 dsRNA antibody J2, red is SARS-CoV-2 nucleocapsid, green is background, and blue is Hoechst
1263 nuclear stain. (U, V, and W) Show individual cells highlighted in T.
1264
1265
1266
1267
1268
1269
1270
1271
1272
1273
1274
1275
1276
1277
1278
1279
1280
1281
1282
1283
1284
1285
1286
1287
1288
1289
1290
1291
1292

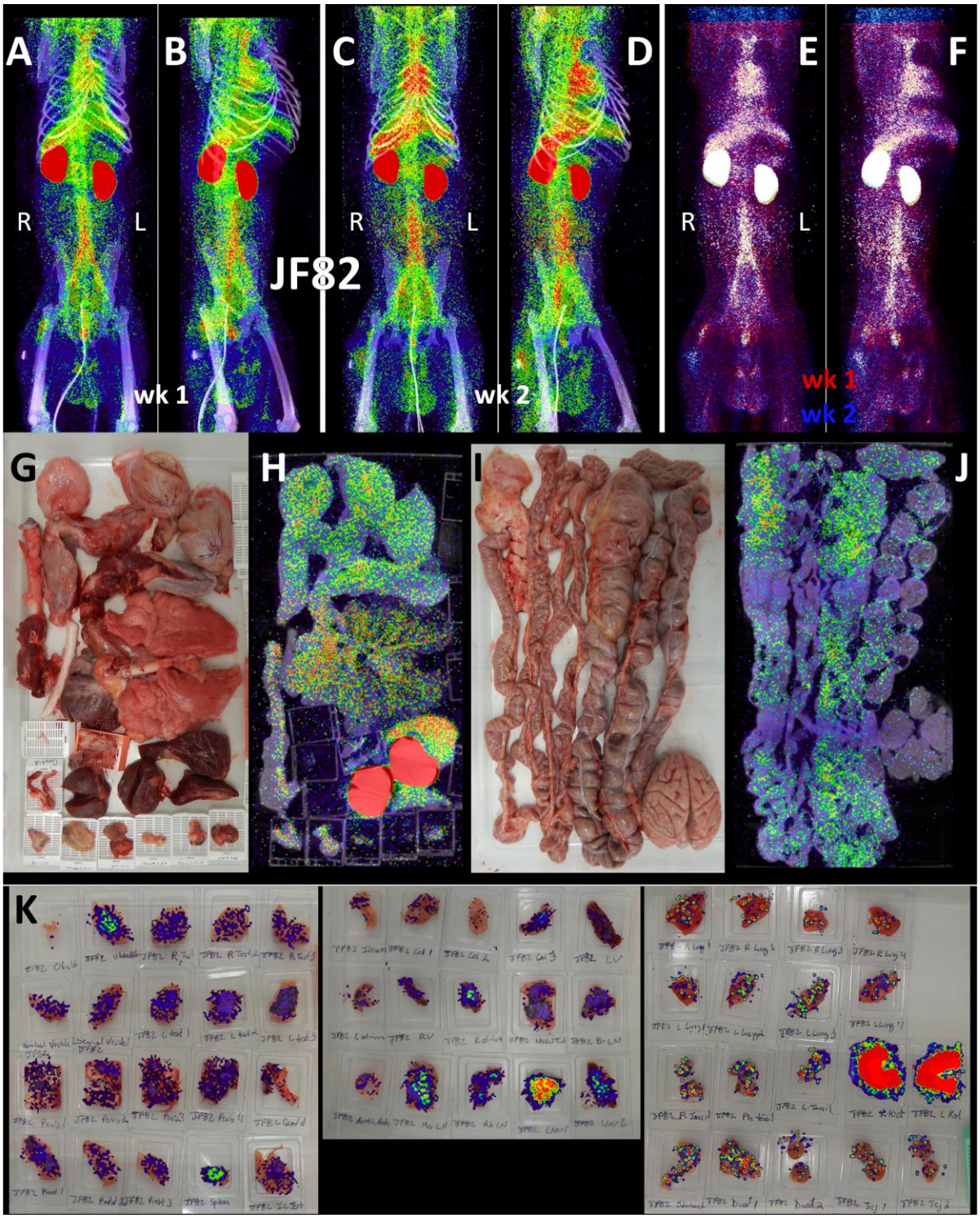

Figure 8. JF82 PET/CT images from week and week 2 necropsy scans. (A and B) Whole-body PET/CT scan of JF82 from 1-week post-infection. Front view (A) and side (B) both shown. (C and D) Whole-body PET/CT scans of JF82 2-weeks post infection. Front view (C) and side (D) both shown. Right and left labeled in front views (A and C). (E and F) Overlay of the week 1 scan

(shown in red) and the week 2 scan (shown in blue). Front (E) and side (F) views both shown. (G) Organ tray post necropsy and (H) PET/CT image. (I) Second organ tray post necropsy and (J) PET/CT image. (K) Overlay of PET signal onto photograph of tissue cassettes.

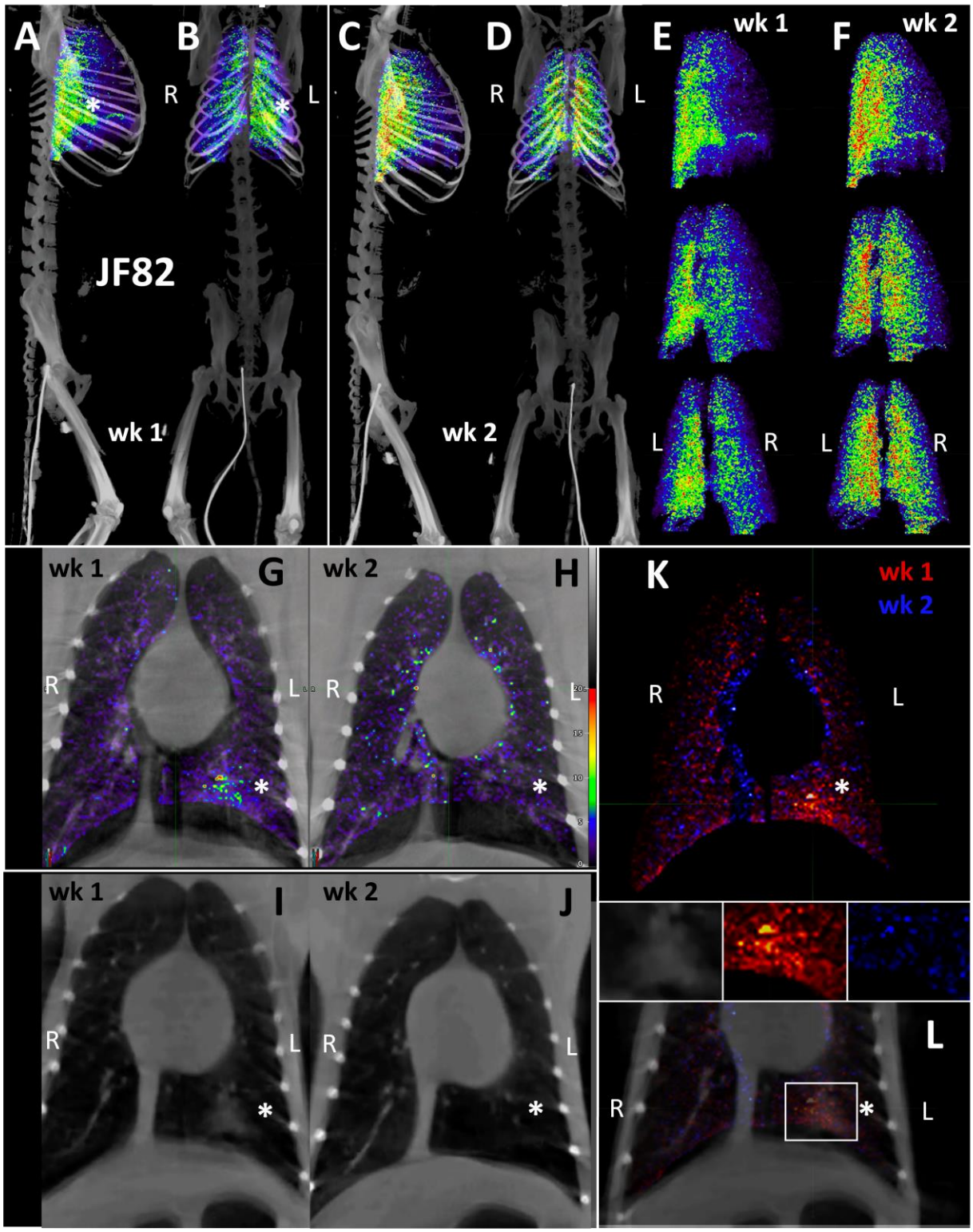

Figure 9. JF82 lung pathology and PET signal from two timepoints. (A-D) Lung PET volumes were isolated and overlaid on whole body CT scans. (A and B) Show lung volumes from 1-wee

scan, side (A) and front (B) views shown. White asterisk indicates location of lung pathology highlighted below. (C and D) Show lung volumes from 2-week scan, side (C) and front (D) views shown. (E and F) Isolated lung PET volumes for each scan are shown independent of CT. (G and H) Overlay of single z-image of PET signal onto single z-image of CT in the lungs at week 1 (G) and week 2 (H). (I and J) Single z-image of CT used in G and H shown independent of PET signal for week 1 (I) and week 2 (J). (K) Overlay of week 1 (shown in red) and week 2 (shown in blue) PET signal. (L) Overlay from K shown with CT image to localize PET signal. Insets above show, CT, week 1, and week 2 signal from left to right. White asterisk indicates location of left lung pathology in all panels.

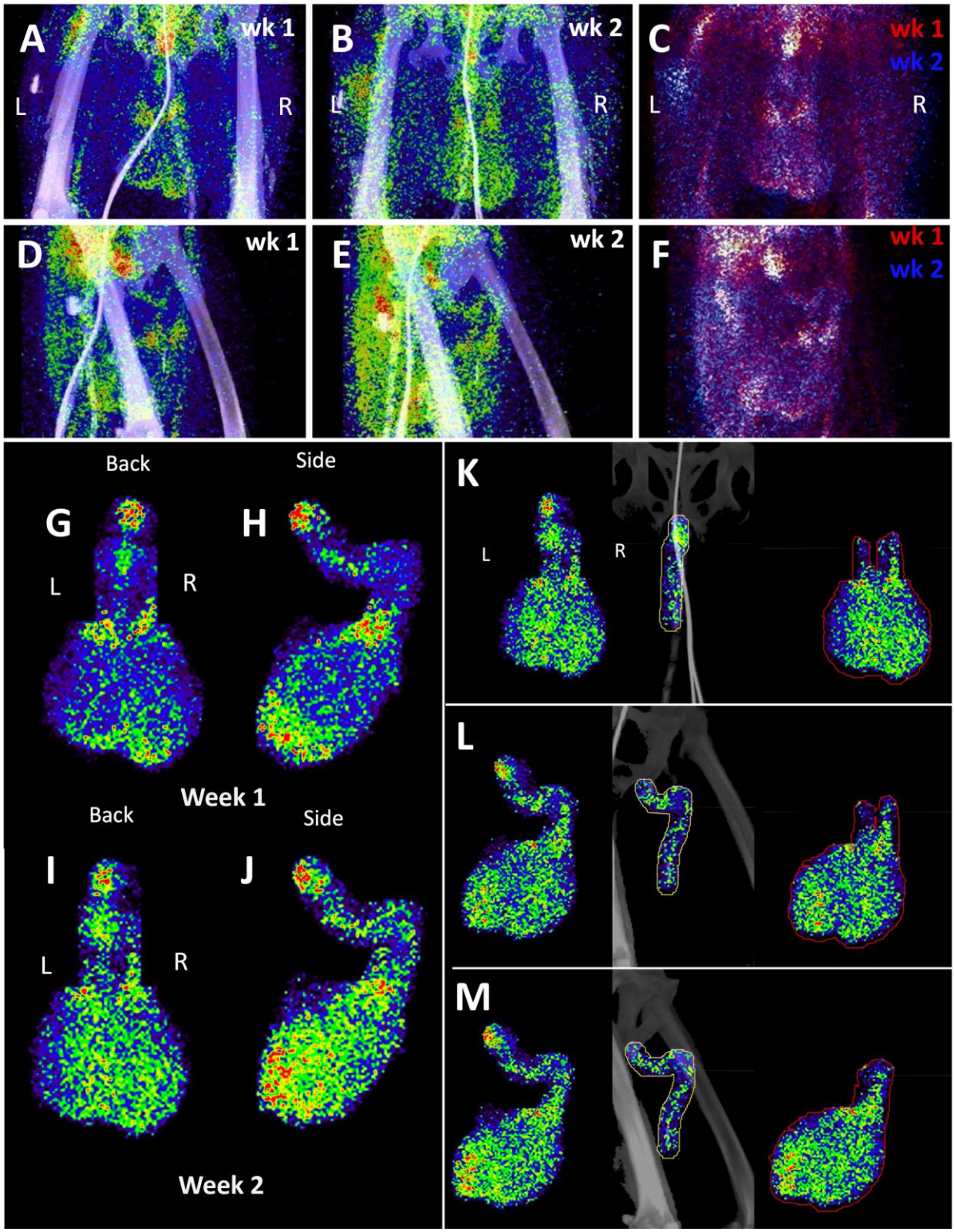
A
wk 1
L
R
B
wk 2
L
R
C
wk 1
wk 2
L
R
D
wk 1
E
wk 2
F
wk 1
wk 2
Back
Side
G
H
L
R
Week 1
Back
Side
I
J
L
R
Week 2
K
L
R
L
M

1354

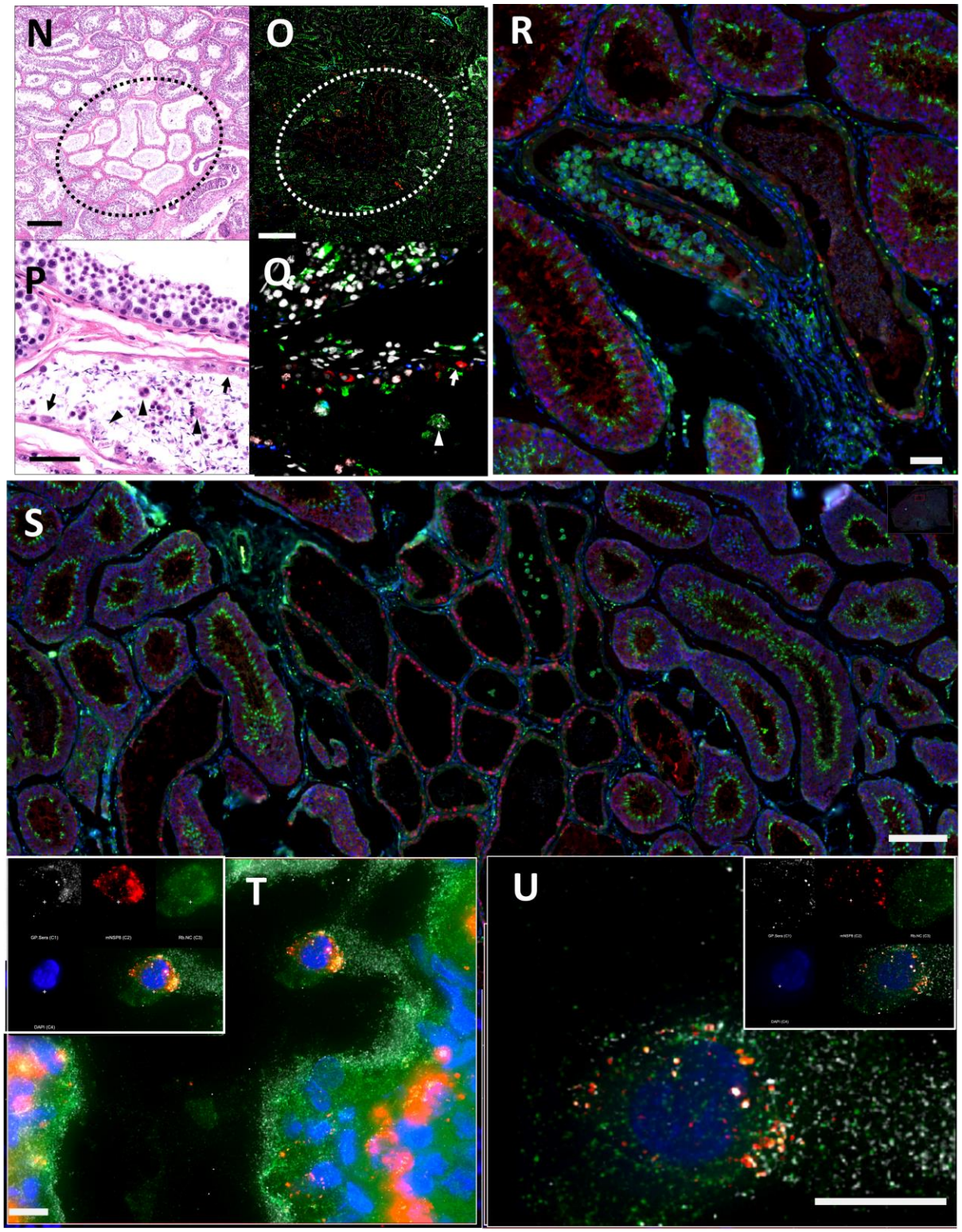

Figure 10. Male genital tract signal in JF82. (A and B) Front view PET/CT images highlighting the lower abdomen of JF82 at 1-week (A) and 2-weeks (B). (C) Overlay of week 1 (shown in red) and week 2 (shown in blue) PET signal. (D and E) Side view of same images shown in A and B. (F)

side view of overlay shown in C. (G and H) Isolated MGT volume from week 1 scan. Back (G) and side (H) views shown. (I and J) Isolated MGT volume from week 2 scan. Back (I) and side (J) views shown. (K, L, and M) Isolated MGT volume from week 2 with isolated penile and testicular signal. Back (K), rotated 45° (L), and side (M) views shown. (N) H&E stain of JF82 testicular tissue. Degenerate seminiferous tubules highlighted in black oval. Scale bar 500 µM. (O) Fluorescent microscopy shows a similar area of degenerate tubules. Green is CD206, red caspase 3, and white nuclear stain. Scale bar 500 µM. (P) Higher magnification image of degenerate tubules. Intraluminal macrophages (arrowheads) and Sertoli cells (arrows) are shown inside tubules. Scale bar 50 µM (Q) Higher magnification of image in O shows Sertoli cells (arrow) staining with caspase 3 and macrophages (arrowhead) staining with CD206. Scale bar 50 µM. (R) Fluorescent microscopy image showing degenerate tubule full of intraluminal macrophages. Red is caspase 3, green is CD206, and blue is nuclear stain. Scale bar 50 µM. (S) Lower magnification microscopy image of degenerate and healthy tubules. Red is caspase 3, green is CD206, and blue is nuclear stain. Scale bar 200 µM. (T and U) Fluorescent microscopy images of infected cells in testicular tissue of JF82. White is SARS-CoV-2 anti-sera, red is NSP8, green is nucleocapsid, and blue is Hoechst nuclear stain. Insets show individual channels, larger image is merge. Scale bars 10 µM.

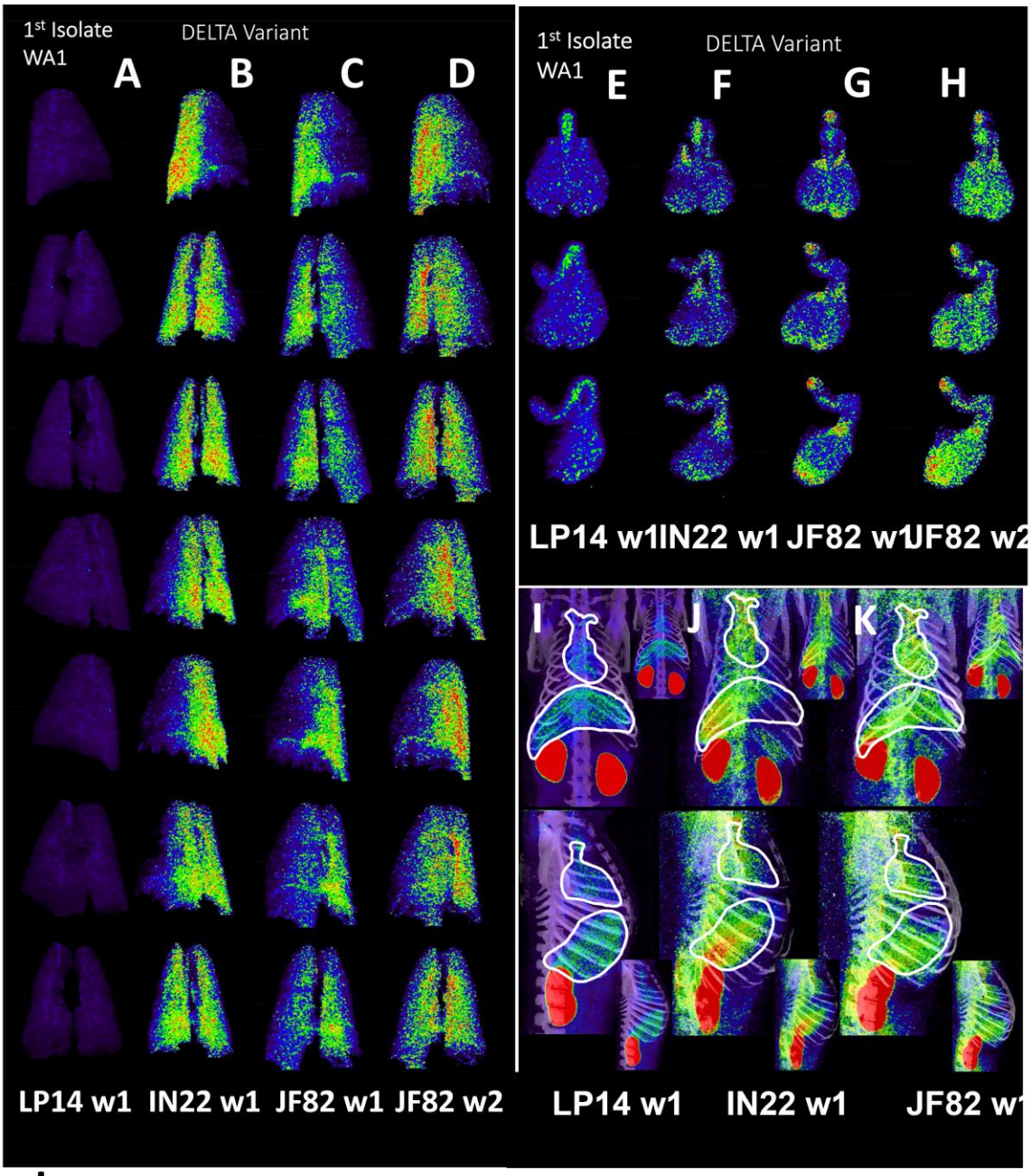
1st Isolate
WA1
DELTA Variant
A
B
C
D
LP14 w1
IN22 w1
JF82 w1
JF82 w2
1st Isolate
WA1
DELTA Variant
E
F
G
H
LP14 w1
IN22 w1
JF82 w1
JF82 w2
I
J
K
LP14 w1
IN22 w1
JF82 w1

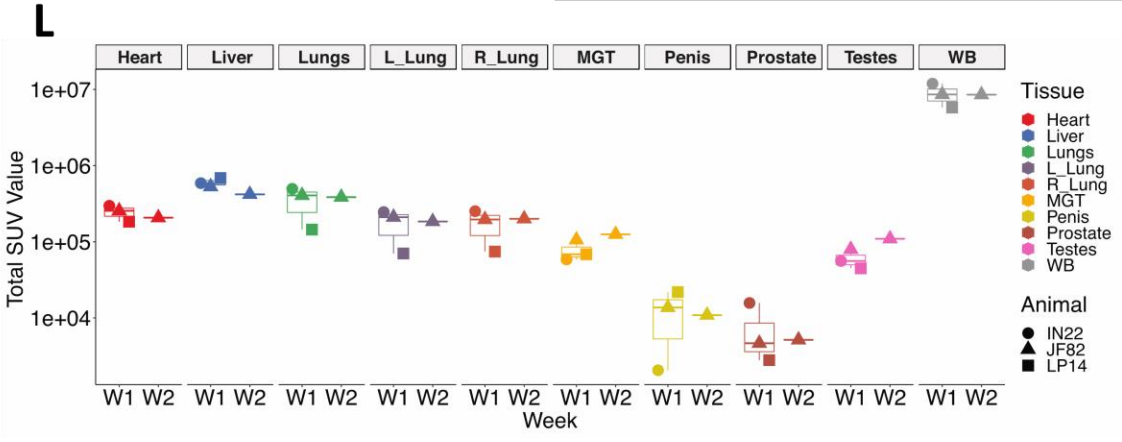
L
Heart
Liver
Lungs
L_Lung
R_Lung
MGT
Penis
Prostate
Testes
WB
Total SUV Value
1e+07
1e+06
1e+05
1e+04
W1 W2
Week
Tissue
Heart
Liver
Lungs
L_Lung
R_Lung
MGT
Penis
Prostate
Testes
WB
Animal
IN22
JF82
LP14

1404

Figure 11. Comparison of SUVs across animals and timepoints. (A-D) Complete rotation series of lung PET volumes for LP14 (A), IN22 (B), JF82 week 1 (C), and JF82 week 2 (D). (E-H) Front, rotated 45°, and side views of MGT PET volumes for LP14 (E), IN22 (F), JF82 week 1 (G), and JF82 week 2 (H). (I-K) Front and side views of whole-body scans, white lines indicate volumes taken for heart and lungs for LP14 (I), IN22 (J), and JF82 week 1 (K). Insets show each image without white outlines. (L) Total SUVs for whole-body scans and each individual volume isolated displayed in graph. Animals are indicated by icon shape and volumes by color.

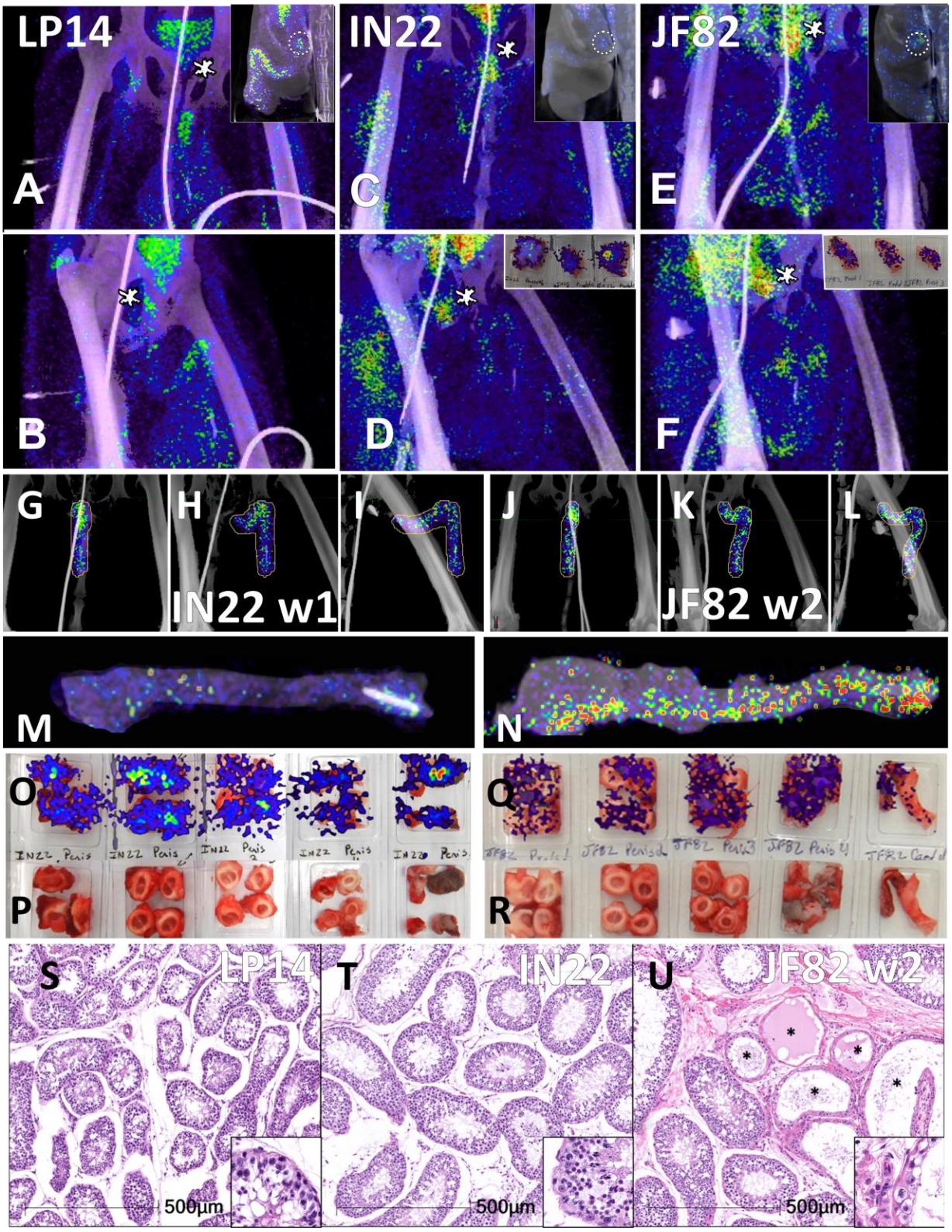

Figure 12. Comparison of prostate and penile signal between animals. (A-F) PET/CT signal in lower abdomen for each animal at 1-week post-infection. LP14 front (A) and rotated 45° (B),

1418 IN22 front (C) and rotated 45° (D), JF82 front (E) and rotated 45° (F). Asterisks mark location of
1419 prostate. Insets show sagittal z-slice of each animal highlighting prostate signal (white circle).
1420 (G-I) PET/CT volume of penis for IN22. Front (G), rotated 45° (H), and side (I) views shown. (J-L)
1421 PET/CT volume of penis for JF82 at 2-weeks post-infection. Front (J), rotated 45° (K), and side (L)
1422 views shown. (M) PET/CT signal of IN22 penis after necropsy. (N) PET/CT signal of JF82 penis
1423 after necropsy. (O) PET/CT signal overlaid onto an image of tissue cassettes (P) containing
1424 penile tissue of IN22. (Q) PET/CT signal overlaid onto an image of tissue cassettes (R) containing
1425 penile tissue of JF82. (S-U) H&E images of testicular tissue from each animal. LP14 (S) and IN22
1426 (T) shows normal spermatogenesis and tissue architecture. IN22 (U) shows degenerate tubules
1427 (asterisks) interspersed among healthy tubules. Scale bars all 500 µM.
1428

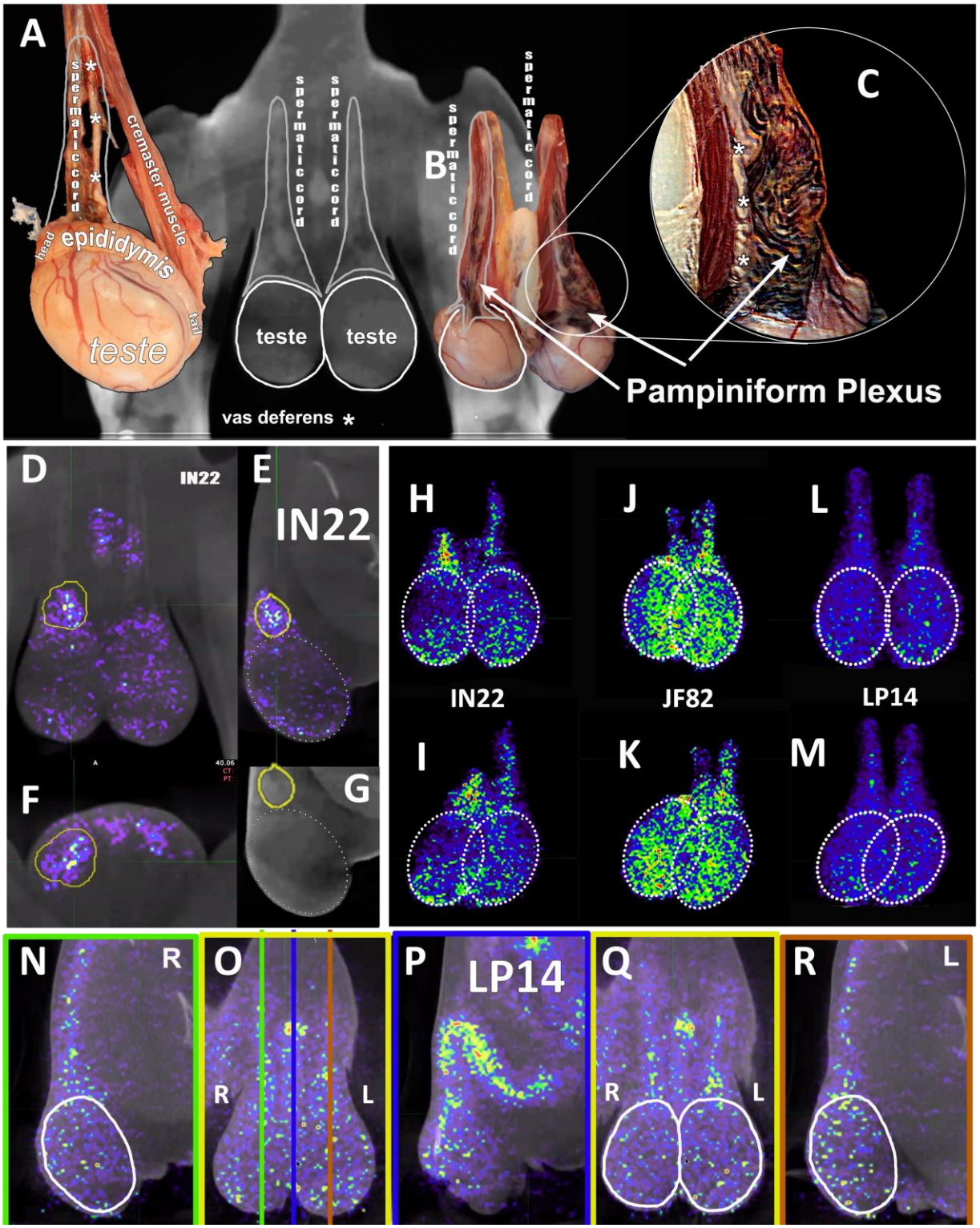

Figure 13. PET signal associated with the pampiniform plexus. (A) Labeled dissection showing anatomical structure of a macaque testis. (B) CT image of testes and associated image showing the matching anatomical features of the spermatic cord. (C) Inset highlighting the location and

appearance of the pampiniform plexus. White asterisks mark the vas deferens in all images. (D-F) Single z PET/CT images of IN22 highlighting the PET signal associated with the pampiniform plexus (yellow volume) from the frontal (D), sagittal (E), and transverse (F) plane. (G) CT image used in E to highlight signal associated with pampiniform plexus (yellow volume). (H-L) Isolated 3D volumes of MGT PET signal shown from the front for IN22 (H), JF82 (J), and LP14 (L). White circles outline testes. (I, K, M) Volumes from H, J, and L rotated 45°. (N) Sagittal z-slice of PET/CT of LP14 showing right testis. (O) Frontal z-slice of PET/CT, colored lines correspond to sagittal slices shown in N, P, and R. (P) Sagittal z-slice of PET/CT showing penile tissue. (Q) Frontal z-slice highlighting the testicular tissue in white ovals. (R) Sagittal z-slice of PET/CT showing left testis of LP14. White ovals highlight signal associated with testes and not pampiniform plexus.

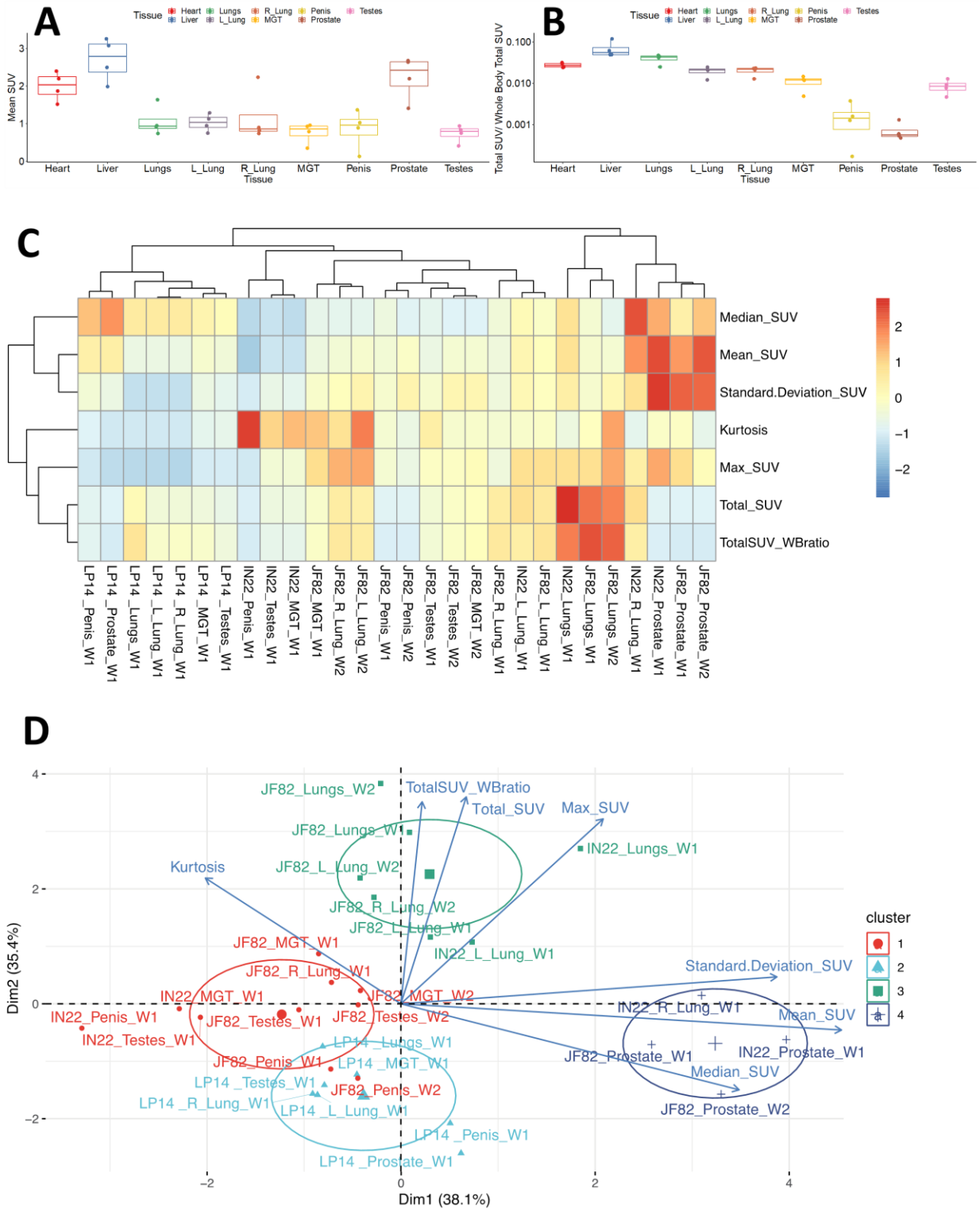

Figure 14. Principle components analysis of SUV measures. (A) Mean SUV values from isolated tissue volumes. (B) The ratio of total SUV for each tissue volume to whole-body total SUV. (C) Heat map showing clustering of tissues and parameters measured from the PET data. (D)

Principal components analysis of measures showing hierarchical clustering of tissues and measures.